

**EFFECTS OF DRAG-REDUCING  
POLYMERS ON TURBULENCE  
GROWTH AND BURSTING IN NEAR  
MINIMAL CHANNELS AND  
EXTENDED DOMAINS**

**EFFECTS OF DRAG-REDUCING  
POLYMERS ON TURBULENCE  
GROWTH AND BURSTING IN NEAR  
MINIMAL CHANNELS AND  
EXTENDED DOMAINS**

BY  
XUE BAI, B.Sc.

A THESIS  
SUBMITTED TO THE SCHOOL OF GRADUATE STUDIES IN PARTIAL FULFILMENT  
OF THE REQUIREMENTS FOR THE DEGREE  
MASTER OF APPLIED SCIENCE

McMaster University© Copyright by Xue Bai, April 2017

**Master of Applied Science (2017)**  
(Chemical Engineering)

McMaster University  
Hamilton, Ontario, Canada

**TITLE:** Effects of drag-reducing polymers on turbulence growth  
and bursting in near minimal channels and extended do-  
mains

**AUTHOR:** Xue Bai, B.Sc.

**SUPERVISOR:** Dr. Li Xi (McMaster University)

**NUMBER OF PAGES:** xvii, 74

# Lay Abstract

Turbulence exists everywhere and can be observed in most fluid flows occurring in nature. To reduce the energy consumption, frictional resistance in the turbulence must be considered in fluid transportation. It has been known since the 1940s that a small amount of long-chain polymer additives can dramatically reduce such drag. The mechanism of drag reduction has attracted extensive attention. Two problems of particular interest are the upper limit of drag reduction (termed maximum drag reduction) and the polymer effects on the laminar-turbulent transition. In this thesis, full transient trajectories from marginal turbulent states towards sustained turbulence in both Newtonian and polymeric flows are monitored by direct numerical simulations. It is observed that polymer additives do not affect the initial growth of turbulence but prevent flows from breaking into strong but small-scale fluctuations afterwards. In a more extended domain, turbulence starts as localized spots which spread across the channel. Adding polymers changes the dynamics of turbulence propagation as well. In addition to the aforementioned problems, this study also sheds lights on the so-called bursting events — intermittent surges in turbulent activities observed in experiments.

# Abstract

Two major problems in viscoelastic turbulence, the effects of polymers on the laminar-turbulent transition dynamics and the origin of the maximum drag reduction asymptote, can be both better understood in the regime near the margin of turbulence. In the first part of this thesis, direct numerical simulation trajectories initiated from the edge state are used to follow its unstable manifold into the turbulent basin. In Newtonian flow, the growth of turbulence starts with the intensification of velocity streaks and a sharp rise in the Reynolds shear stress. It is followed by a quick breakdown into high-intensity small-scale fluctuations before entering the core of turbulence. Adding drag-reducing polymers does not affect the initial growth of turbulence but stabilizes the primary streak-vortex structure, which help the flow circumvent the breakdown stage. Throughout the process, polymers act in reaction to the growing turbulence and do not drive the instability. This part not only reveals the transition dynamics into turbulence but also presents a comprehensive view of the bursting stage observed in the near-wall self-sustaining cycle, which starts as the flow leaves hibernating turbulence and is redirected towards the turbulent basin by the unstable manifold of the edge state.

On the other hand, this thesis also discusses the effects of polymer addition on the

laminar-turbulent transition in extended domains. Localized turbulent spot can be clearly observed in the large box, and this turbulent region will spread as well as tend to “split” but finally fill up the whole domain before it is separated. Polymers don’t affect the flow dynamics until the burst. Similarly, vortex structures rapidly break down into small scales after the first bursting of Reynolds shear stress, but polymer additives depress this process.

The thesis offers a clear and comprehensive overview of the transition into turbulence in the presence of drag-reducing polymers. Future work remains in two major directions. The first is to pinpoint the flow states responsible for the quantitative origin of the universal upper limit of drag reduction observed in experiments. The second is to determine the role, if any, of elasticity-driven instabilities in the transition.

# Acknowledgements

Firstly, I would like to express my sincere appreciation to my supervisor, Dr. Li Xi. Without his patient guidance and continuous encouragement, it's impossible for me to complete this thesis. I am also grateful to other faculty members of Department of Chemical Engineering and all the lectures in the School of Engineering. Especially thank Dr. Carlos Filipe, Dr. David Latulippe and Dr. Marilyn Lightstone for their assistance to my study completion.

I would like to acknowledge all the members of Dr. Li Xi's group. Special thanks go out to Lu Zhu, who helped me a lot in running simulations for extended domains. Also thanks to other friends I met in McMaster University, I have been encouraged so much during my study.

There is also gratitude to the Natural Sciences and Engineering Research Council of Canada (NSERC) for financial support of the projects, and the Shared Hierarchical Academic Research Computing Network (SHARCNET) and Compute/Calcul Canada for the facilities used to run computational tasks.

Finally, I would like to thank my family for their unconditional support and love. The solid backing from them always inspired me to endeavor.

# Contents

<b>Lay Abstract</b>	<b>iii</b>
<b>Abstract</b>	<b>iv</b>
<b>Acknowledgements</b>	<b>vi</b>
<b>List of Tables</b>	<b>ix</b>
<b>List of Figures</b>	<b>x</b>
<b>List of Abbreviations and Symbols</b>	<b>xv</b>
<b>1 Introduction</b>	<b>1</b>
<b>2 Methodology</b>	<b>8</b>
2.1 Formulation and simulation details . . . . .	8
2.2 Numerical edge tracking . . . . .	12

<b>3</b>	<b>Results and Discussion</b>	<b>17</b>
3.1	Studies on the near minimal flow unit . . . . .	17
3.1.1	Overview . . . . .	17
3.1.2	Mean velocity development and shear stress balance . . . . .	23
3.1.3	Flow structure development . . . . .	30
3.1.4	Turbulence growth and polymer effects . . . . .	36
3.1.5	Initial condition dependence . . . . .	41
3.2	Studies on the large domain . . . . .	45
3.2.1	Flow structure development . . . . .	45
3.2.2	Analysis based on conditional average . . . . .	58
<b>4</b>	<b>Conclusions</b>	<b>63</b>

# List of Tables

1	Numerical details for domain $L_x^+ \times L_z^+ = 720 \times 230$ . For all the simulations, $N_y = 145$ , $\delta_{y,\min}^+ = 0.025$ and $\delta_{y,\max}^+ = 2.28$ . . . . .	11
2	Numerical details for domain $L_x^+ \times L_z^+ = 8000 \times 800$ . . . . .	12

# List of Figures

1.1	Schematic of the state space of invariant and transient solutions to the Navier-Stokes equation. . . . .	4
2.1	The plane Poiseuille geometry. . . . .	9
2.2	Time series of the bulk-averaged TKE of the twin trajectories used in edge tracking ( $Wi = 28$ ). Solid and dashed lines are for trajectories on the turbulent and laminar side, respectively; round dots indicate the points of bisection (see text) . . . . .	13
2.3	Time series of the bulk-averaged TKE of the twin trajectories used in edge tracking (Newtonian, $L_x^+ \times L_z^+ = 8000 \times 800$ ). Solid and dashed lines are for trajectories on the turbulent and laminar side, respectively; round dots indicate the points of bisection. . . . .	15
2.4	Vortex configuration for ES: (a) domain size: $L_x^+ \times L_z^+ = 4000 \times 800$ ; (b) domain size: $L_x^+ \times L_z^+ = 8000 \times 800$ . The isosurface of $Q = Q_{\text{rms}}$ is shown, where $Q_{\text{rms}}$ is the root mean square of the Q field. . . . .	16

3.1	Time series of shooting trajectories initiated from the ES: (a) Newtonian; (b) $Wi = 100$ . The blue solid line (left axis) shows peak values of instantaneous RSS profile; the green dash line (1st right axis) shows bulk-average TKE; the red dotted line (2nd right axis) shows bulk average of $\alpha_{yy} + \alpha_{zz}$ . . . . .	18
3.2	Time series of the turbulent core at $Wi = 40$ : the blue solid line (left axis) shows peak values of instantaneous RSS profiles; the green dash line (right axis) shows bulk-average TKE $k_b$ . . . . .	19
3.3	State-space projection of solution trajectories. Moments I~IV on the $Wi = 100$ trajectory are labeled in fig. 3.1(b). . . . .	22
3.4	Mean velocity profiles: (a) time-average profiles for Newtonian and viscoelastic cases (at the SCS); (b) instantaneous profiles for initial condition and moments I~IV (as labeled in fig. 3.1; $Wi = 100$ ) during the transient development (dot-dashed: viscous sublayer; dashed: PvK log law; dotted: Virk log law). . . . .	24
3.5	Contributions to the mean velocity gradient development according to (3.5) (left) and the log-law slope $A_{25}^*$ (right) for $Wi = 100$ . Horizontal reference lines are added at the 0 mark of the left axis and the $A_{\text{text}} = 11.7$ mark of the right axis; the vertical reference line marks the moment when $A_{25}^* = A_{\text{VirK}}$ . Time axis matches that of fig. 3.1. . . . .	26
3.6	Contributions to the total shear stress in the Newtonian case: (a)~(e) – moments I~V; black dot-dashed line is the steady-state TSS ((3.7)).	28

3.7	Contributions to the total shear stress in the $Wi = 100$ case: (a) initial condition; (b)~(f) – moments $I \sim V$ ; black dot-dashed line is the steady-state TSS ((3.7)). . . . .	29
3.8	Streamwise velocity distribution at $y^+ = 24.85$ for the Newtonian case: (a)~(e) – Moments $I \sim V$ ; the color ranges from black to white for 0 to 1. 31	31
3.9	Streamwise velocity distribution at $y^+ = 24.85$ for the $Wi = 100$ case: (a) initial condition; (b)~(f) Moments $I \sim V$ ; the color ranges from black to white for 0 to 1. . . . .	32
3.10	Vortex configuration for the Newtonian case: (a)–(e) are moments $I \sim V$ ; the isosurface of $Q = Q_{rms}$ is shown, where $Q_{rms}$ is the root mean square of the $Q$ field. . . . .	34
3.11	Vortex configuration for the $Wi = 100$ case: (a) initial conditions and (b)–(f) are moments $I \sim V$ ; the isosurface of $Q = Q_{rms}$ is shown (in (a) $Q = 4.0Q_{rms}$ ), where $Q_{rms}$ is the root mean square of the $Q$ field. . . . .	35
3.12	TKE and RSS budgets for the Newtonian case: (a)–(e) are moments $I \sim V$ . . . . .	39
3.13	TKE and RSS budgets for the $Wi = 100$ case: (a) initial condition; (b)–(f) are are moments $I \sim V$ . . . . .	40
3.14	Time series of the transient growth of turbulence from the initial disturbance of (3.13) in Newtonian flow. The green dash line (left axis) shows bulk-average TKE; the blue solid line (right axis) shows peak values of instantaneous RSS profile. . . . .	43

3.15	State-space projection of transient DNS trajectories initiated from the ES and from the imposed disturbance of (3.13). . . . .	43
3.16	Streamwise velocity distribution at $y^+ = 24.85$ for the transient development of Newtonian turbulence initiated from the imposed disturbance of (3.13): (a) is the initial disturbance; (b)–(f) are moments i–v labeled in fig. 3.14 . . . . .	44
3.17	Vortex configuration for the Newtonian case: (a)–(g) are moments I–VII; the isosurface of $Q = Q_{\text{rms}}$ is shown, where $Q_{\text{rms}}$ is the root mean square of the $Q$ field. . . . .	47
3.18	Vortex configuration for $Wi = 64$ case: (a)–(f) are moments I–VI; the isosurface of $Q = Q_{\text{rms}}$ is shown in red, where $Q_{\text{rms}}$ is the root mean square of the $Q$ field; the isosurface of $\alpha_{yy} + \alpha_{zz} = 0.2(\alpha_{yy} + \alpha_{zz})_{\text{max}}$ is shown in blue. . . . .	49
3.19	The spatiotemporal distribution of $Q$ : (a)Newtonian; (b) $Wi = 64$ . The color ranges from black to white for 0 to 1.4 (a) and 0.75 (b), respectively.	52
3.20	Streamwise velocity distribution at $y^+ = 24.85$ for the Newtonian case: (a)~(g) – Moments I~VII; the color ranges from black to white for 0 to 1. Red lines indicate the boundary of laminar-turbulent regions. . .	53
3.21	Streamwise velocity distribution at $y^+ = 24.85$ for $Wi = 64$ case: (a)~(f) – Moments I~VI; the color ranges from black to white for 0 to 1. Red lines indicate the boundary of laminar-turbulent regions.	54

3.22	Time series of shooting trajectories initiated from the ES for $L_x^+ \times L_z^+ = 8000 \times 800$ domains (conditional average): (a) Newtonian; (b) $Wi = 64$ . The blue solid line (left axis) shows peak values of instantaneous RSS profile; the green dash line shows bulk-average TKE. . . . .	56
3.23	Mean velocity instantaneous profiles (conditional averaged): (a) Newtonian; (b) $Wi = 64$ . The darker red lines indicate earlier moments and lighter yellow lines indicate later moments. All moments are marked in fig. 3.22. Dot-dashed: viscous sublayer; dashed: PvK log law; dotted: Virk log law. . . . .	57
3.24	Contributions to the total shear stress (conditional averaged, bottom wall) in the Newtonian case: (a)~(g) – moments I~VII. . . . .	60
3.25	Contributions to the total shear stress (conditional averaged, bottom wall) in $Wi = 64$ case: (a)~(f) – moments I~VI. . . . .	61

# List of Abbreviations and Symbols

DR	drag reduction
ES	edge state
PIV	particle image velocimetry
DNS	direct numerical simulation
MDR	maximum drag reduction
L-T	laminar-turbulent
$U_m$	mean velocity normalized by the friction velocity
$y^+$	distance from the wall normalized by the viscous length scale
EIT	elasto-inertia turbulence
Re	Reynolds number
$Re_{crit}$	critical Reynolds number
MFU	minimal flow unit
UB	upper-branch
LB	low-branch
x,y,z	Cartisian coordinate
t	time
p	pressure
$l$	half-channel height

$U_{CL}$	Newtonian laminar center-line velocity
$\rho$	density
FENP	finitely extensible nonlinear elastic dumbbell model with the Peterlin approximation
$\eta$	zero-shear-rate viscosity
Wi	Weissenburg number
$\lambda$	polymer relaxation time
$\beta$	viscosity ratio
$\tau_w$	wall shear stress
$u_\tau$	friction velocity
$\delta_v$	viscous length scale
$Re_\tau$	friction Reynolds number
$\boldsymbol{\tau}_p$	polymer shear stress tensor
$\boldsymbol{\alpha}$	polymer conformation tensor
$\text{tr}(\mathbf{A})$	trace of tensor $\mathbf{A}$
$\mathbf{Q}$	end-to-end vector of polymer molecule
b	polymer extension limit
$\boldsymbol{\delta}$	Kronecker delta tensor
$N_y$	Chebyshev modes
$\delta^+$	unit length normalized by the viscous length scale
CFL	Courant-Friedrichs-Lewy
$\delta_t$	time step size
Sc	Schmidt number
TKE	turbulent kinetic energy
$k_b$	bulk-averaged turbulent kinetic energy
$v'$	velocity fluctuation

---

Q	vortex strength
rms	root-mean square
TU	time unit
RSS	Reynolds shear stress
SCS	statistically-converged stage
A	local log-law slope
PvK	Prandtl-von Kármán
TSS	total shear stress
VSS	viscous shear stress
PSS	polymer shear stress
$\Omega$	vorticity tensor
$\Gamma$	rate of strain tensor
$\mathcal{P}$	production
$\epsilon_v$	viscous dissipation
$\epsilon_p$	conversion into elastic energy
$\mathcal{R}$	pressure-rate-of-strain
I.C.	initial condition
$\overline{Q_{xz}}$	vortex strength averaged along wall-normal direction

# Chapter 1

## Introduction

The transition from a laminar flow to turbulence is accompanied by an abrupt increase in the friction drag of the flow. Long-chain flexible polymer additives are known to cause significant drag reduction (DR) even at very low concentrations [62, 19, 69, 20]. Much progress has been made in the fundamental understanding of the DR phenomenon since its initial discovery in the 1940s [61], especially during the past 20 years when tools providing direct access to turbulent flow fields, including particle image velocimetry (PIV) [66, 70] and direct numerical simulations (DNS) [59, 38, 9], were broadly applied in this field. In particular, although the exact mechanism of DR remains debatable [69], it is now generally accepted that polymers suppress turbulence by counteracting the vortical motions therein [6, 10, 37, 34]. However, behaviors of viscoelastic turbulent flows remain puzzling in two major areas: the maximum drag reduction (MDR) and laminar-turbulent (L-T) transition.

MDR is widely regarded as the most important unsolved problem in viscoelastic turbulence. As the polymer-induced elasticity increases, the level of DR initially increases

but eventually saturates to the MDR asymptote, whose magnitude is insensitive to polymer species, molecular weight, or concentration [62]. MDR mean velocity profiles from experiments with different polymer solutions and pipe diameters were found to follow the same Virk [62] log-law relationship:

$$U_m^+ = 11.7 \ln y^+ - 17.0 \quad (1.0)$$

(the superscript “+” denotes quantities non-dimensionalized in turbulent inner scales[46]; further explained below in chapter 2), once MDR is reached. The Virk log-law is commonly cited as the quantitative indicator of MDR, which also applies to channel (Poiseuille) flow [65]. In addition to its quantitative magnitude, any theory attempting to explain MDR must address simultaneously its existence and universality. The existence of MDR, that polymers are not able to completely quench turbulence but only push it towards an asymptotic limit, indicates that there must be a unique mechanism for sustaining turbulence. This is further supported by the observation of distinct flow structures at MDR compared with those of Newtonian turbulence [66, 70, 26, 36, 73]. Its universality with respect to changing polymer solution properties, meanwhile, is highly counter-intuitive, as MDR is typically reached at the limit of strong polymer effects. Earlier theoretical attempts at explaining MDR are phenomenological or semi-empirical in nature [62, 57, 47] and have met contradictory evidences as new experimental and numerical data emerged (see discussion in White and Mungal [69], Xi and Graham [78].) A mechanistic theory that consistently explains all three key aspects of MDR – its existence, universality, and Virk log law – is still missing.

As to the L-T transition, since polymers can suppress turbulent fluctuations, it is intuitive to expect that the transition will be delayed to a higher Re compared with Newtonian flow, which was indeed often observed in experiments [18, 7, 15]. However,

early transition was also reported for certain experimental conditions [49, 21]. This complex dependence on polymers suggests the coexistence of more than one transition pathway. Recent experiments by Samanta *et al.* [51] showed that as the polymer concentration increases, the origin of the instability driving the transition changes from inertia – the same transition mechanism as Newtonian flow which is only delayed by polymers – to a combination of inertia and elasticity. The latter so-called “elasto-inertial turbulence (EIT)” can appear at  $Re$  much lower than  $Re_{crit} \approx 2100$  of the Newtonian pipe flow and shows distinct flow structures from the coherent structures in inertia-driven turbulence [11].

In Newtonian channel flow, the transition to turbulence bypasses the Tollmien-Schlichting (T-S) wave, which does not appear until  $Re \approx 5600$  [29], and is able to occur at a much lower  $Re_{crit} \approx 1000$  [40] and higher turbulence growth rate [27, 14]. DNS has been extensively used in the study of Newtonian bypass transition. The process starts with extended streamwise velocity streaks whose instability leads to a quick “breakdown” process, from which vortical structure and three-dimensional turbulence is generated [23, 79, 52, 71, 72]. Much less is known about the transition process in viscoelastic fluids. Earlier studies all focused on the linear stability analysis [24, 25, 82, 43]. To our best knowledge, the only full nonlinear DNS study of the L-T transition process reported so far is that by Agarwal *et al.* [1], where the development of a localized perturbation was tracked and polymers were found to suppress the turbulence growth rate and prolong the transition process.

From a dynamical system perspective, at the moderate  $Re$  where we focus, there are two basins of attraction in the solution state space of the Navier-Stokes equation (fig. 1.1). The laminar state is a linearly stable steady state whereas turbulence can be viewed as a chaotic attractor formed around a number of invariant saddle points [17, 5].

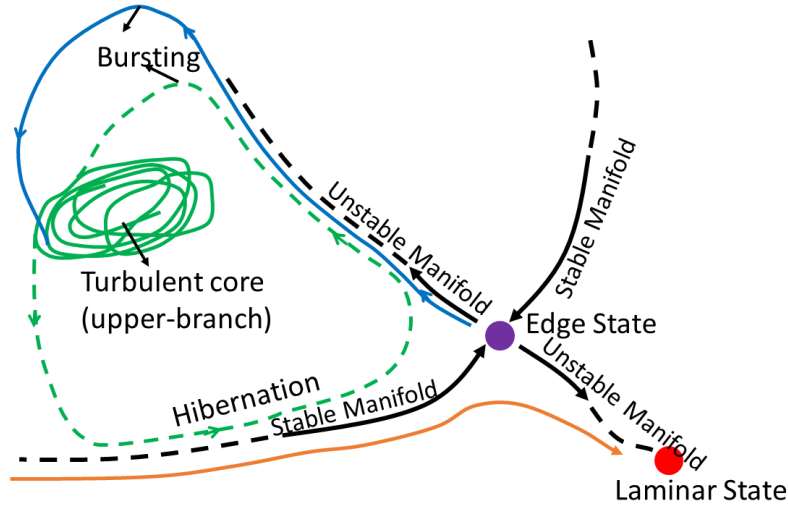


Figure 1.1: Schematic of the state space of invariant and transient solutions to the Navier-Stokes equation.

In the context of L-T transition, one saddle point of particular interest is the so-called edge state (ES) [56, 53], whose stable manifold forms the boundary between the basins. Dynamical trajectories initiated from different sides of the boundary head towards opposite directions, following the unstable manifold of the ES. To trigger turbulence from the laminar state, the disturbance must be large enough to overpass the L-T boundary. The importance of the ES in governing the L-T transition is clearly illustrated in a recent study of the asymptotic boundary layer flow, where the transient development of turbulence triggered by random noises was found to be mediated by the ES and its stable and unstable manifolds [32].

From the perspective of the turbulent basin, the ES is the most marginal form of self-sustaining turbulence since any states with a weaker form of perturbation will decay to the laminar state. Therefore, with the increasing elasticity caused by polymer additives, it is natural to ask what happens to the ES and what role it plays in keeping turbulence self-sustaining, which is eventually fundamental to our understanding

of MDR. Numerical solutions of the ES in viscoelastic flow were only computed recently [77, 74]. Flow structures of these flow states are strongly reminiscent of those of MDR, which feature smooth velocity streaks, weak vortices, and a kinematics dominated by shear [74]. As a result, polymer molecules are not sufficiently stretched and the polymer stress is limited; consequently, the flow statistics of the ES is confirmed to be insensitive to polymer effects. Existence of weak but self-sustaining turbulent states unaltered by drag-reducing polymers not only explains the existence of MDR – i.e., why polymers are not able to completely quench turbulence to the laminar state, it also offers a perfect explanation to the universality of MDR: these weak turbulence states are intrinsically Newtonian whose flow statistics are not affected by polymers. Meanwhile, the quantitative origin of the Virk asymptote remains unsolved. Although the ES mean velocity follows the Virk log law in one particular case [77], departure from the asymptote was observed with changing  $Re$  and domain size [74]. Most likely, the ES is not the single state governing the dynamics at MDR.

Indeed, a group of states with quiescent turbulent dynamics, weak polymer stretching, and MDR-like flow structures were identified from DNS solutions in minimal flow units (MFUs), which were collectively termed “hibernating” turbulence in a series of recent studies [75, 78, 64]. As sketched in fig. 1.1 with a green line, a dynamical trajectory spends most of its time sampling the region near the upper-branch (UB) traveling wave solutions, which forms the core of strong “active” turbulence. Hibernating turbulence occurs when excursions are made towards the low-branch (LB) solutions [44], which were known to form the ES [63]. Transition to hibernating turbulence is rare in the Newtonian flow, but polymers are able to suppress active turbulence and increase the frequency of hibernation, leading to a flow that increasingly resembles MDR. Taking an ergodic view of turbulent dynamics, this intermittent transition between active and

hibernating intervals in an MFU is translated to spatial intermittency showing active and hibernating patches in larger domains, which is confirmed in recent experimental and simulation studies [68, 35].

It becomes increasingly clear that the key to understanding both the MDR and L-T transition of viscoelastic flow lies in the region around the ES. In this study, we explore this region by shooting DNS trajectories initiated from the ES and tracking their dynamics leading to the turbulent basin (see the blue line in fig. 1.1). Compared with traditional DNS, this approach allows us to control the direction of the dynamical trajectories and systematically study the polymer effects on the development of turbulent coherent structures from their most marginal state. This is also what differs our approach from that of Agarwal *et al.* [1], which used an arbitrary initial disturbance on the laminar base flow. In addition, our focus is not on the growth rate of an initial disturbance, but on the evolution mechanism of coherent structures.

Firstly, we use a simulation domain close to an MFU, not only because the cost of computing ES solutions is much higher than DNS and a small-domain ES solution was available from our earlier study [74], but also because the MFU approach separates the temporal evolution from spatial intermittency and allows us to focus on the former [30, 76]. Note from fig. 1.1 that in addition to the L-T transition, our shooting trajectory also closely accompanies the transition pathway from hibernating turbulence back to the turbulent core: this study will also shed light on the fundamental mechanism behind the active-hibernating shifting dynamics, which as shown earlier is important for understanding the convergence towards MDR [75, 78]. Finally, as discussed above, the ES alone does not provide an explanation to the quantitative origin of the Virk asymptote [74]: searching its surrounding region is a natural next step.

Secondly, totally different vortex configuration will be observed in an extended domain. A spotlike turbulent region can be highly localized if the box size is large enough, no matter in Couette flow or in Poiseuille flow[13, 55, 50, 80], and people were concerned about such localized state at the L-T boundary. Attention was paid on the L-T transition[13, 55], but further monitor to the comparison of the Newtonian and viscoelastic extended cases remains blank yet. Here, we will not only detail the whole transient process initiated from ES towards turbulence but also compare the Newtonian case with polymer-introduced case.

# Chapter 2

## Methodology

### 2.1 Formulation and simulation details

We focus on flow in the plane Poiseuille geometry (fig. 2.1) driven by a constant mean pressure gradient. The  $x$ ,  $y$  and  $z$  coordinates are the streamwise, wall-normal and spanwise directions respectively. Lengths are scaled with the half-channel height  $l$ , velocities are scaled with Newtonian laminar center-line velocity  $U_{CL}$ , time is scaled with  $l/U_{CL}$ , and pressure is scaled with  $\rho U_{CL}^2$ . The no-slip boundary condition is applied at the walls ( $y = \pm l$ ) and periodic boundary conditions are adopted in  $x$  and  $z$  directions, in which the periods are denoted as  $L_x$  and  $L_z$ .

The conservation equations of momentum and mass are:

$$\frac{\partial \mathbf{v}}{\partial t} + \mathbf{v} \cdot \nabla \mathbf{v} = -\nabla p + \frac{\beta}{\text{Re}} \nabla^2 \mathbf{v} + \frac{2(1-\beta)}{\text{ReWi}} (\nabla \cdot \boldsymbol{\tau}_p), \quad (2.1)$$

$$\nabla \cdot \mathbf{v} = 0. \quad (2.1)$$

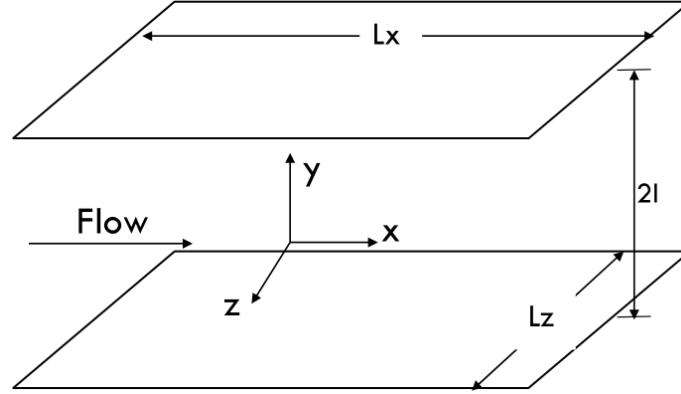


Figure 2.1: The plane Poiseuille geometry.

Here, the Reynolds number is defined as  $Re \equiv \rho U_{CL} l / \eta$ , where  $\rho$  is the total density of the fluid;  $\eta \equiv \eta_s + \eta_p$  is the total zero-shear-rate viscosity of the fluid and  $s$  and  $p$  represent solvent and polymer contributions respectively. The Weissenberg number is defined as  $Wi \equiv 2\lambda U_{CL} / l$ , the product of the polymer relaxation time  $\lambda$  and the mean wall shear rate. The viscosity ratio  $\beta \equiv \eta_s / (\eta_s + \eta_p)$  is the ratio of the solvent viscosity to the total zero-shear-rate viscosity, and  $1 - \beta$  is approximately proportional to the polymer concentration in dilute polymer solutions. We can use  $\rho$ ,  $\eta$  and the mean wall shear stress  $\tau_w$  to define turbulent inner scales, which are more appropriate in the near-wall region [46]. Therein, velocity is scaled with friction velocity  $u_\tau \equiv \sqrt{\tau_w / \rho}$ , and the viscous length scale  $\delta_v \equiv \eta / \rho u_\tau$ . Then the friction Reynolds number is defined as  $Re_\tau \equiv \rho u_\tau l / \eta$  and the eddy turnover time is  $l / u_\tau$ . Quantities nondimensionalized with these time-averaged inner scales are marked with a superscript “+”. Because of the constant mean wall shear stress,  $Re_\tau = \sqrt{2Re}$  and  $l / u_\tau = \sqrt{Re} / 2$  are both constant. Following earlier studies [75, 78, 77, 74], for flow fields and statistics near one of the walls in an instantaneous snapshot, it is more relevant to use the wall shear stress of that wall and at that moment,  $\tau_w^*$ , to define the inner scales; quantities scaled in this way are marked with a superscript “\*”.

In (2.1), the last term on the right-hand side contains the polymer stress tensor  $\boldsymbol{\tau}_p$ , which is obtained from the FENE-P constitutive equation (finitely extensible nonlinear elastic dumbbell model with the Peterlin approximation) [4]:

$$\begin{aligned} \frac{\boldsymbol{\alpha}}{1 - \frac{\text{tr}(\boldsymbol{\alpha})}{b}} + \frac{\text{Wi}}{2} \left( \frac{\partial \boldsymbol{\alpha}}{\partial t} + \mathbf{v} \cdot \nabla \boldsymbol{\alpha} - \boldsymbol{\alpha} \cdot \nabla \mathbf{v} - (\boldsymbol{\alpha} \cdot \nabla \mathbf{v})^T \right) \\ = \left( \frac{b}{b+2} \right) \boldsymbol{\delta}, \end{aligned} \quad (2.1)$$

$$\boldsymbol{\tau}_p = \frac{b+5}{b} \left[ \frac{\boldsymbol{\alpha}}{1 - \frac{\text{tr}(\boldsymbol{\alpha})}{b}} - \left( \frac{b}{b+2} \right) \boldsymbol{\delta} \right]. \quad (2.1)$$

Here  $\boldsymbol{\delta}$  is the Kronecker delta tensor. With  $\mathbf{Q}$  denoting the end-to-end vector of polymer molecules, the conformation tensor is defined as  $\boldsymbol{\alpha} \equiv \langle \mathbf{Q}\mathbf{Q} \rangle$  ( $\langle \cdot \rangle$  represents the ensemble average). The polymer extension is limited by an upper limit  $b$ :  $\max(\text{tr}(\boldsymbol{\alpha})) < b$ . In total, the system is specified by four parameters  $\text{Re}$ ,  $\text{Wi}$ ,  $\beta$  and  $b$ . All simulations reported in this study are performed at a moderate  $\text{Re} = 3600$  ( $\text{Re}_\tau = 84.85$ ). Although most experiments are performed at much higher  $\text{Re}$ , the evidence is abundant that qualitative transitions in viscoelastic turbulence can all be observed in the regime close to the L-T transition [62, 76, 20]. On the other hand, because of the high numerical resolution required to capture the initial stage of turbulence growth (discussed below), the computational cost can quickly become prohibitive as  $\text{Re}$  increases. All viscoelastic cases reported have the same  $\beta = 0.97$  and  $b = 5000$  and cover three different  $\text{Wi}$  in near MFUs: 28, 40, and 100, one in extended domain: 64.

The equation system is discretized with a Fourier-Chebyshev-Fourier pseudo-spectral scheme in space and integrated in time with a third-order semi-implicit backward-differentiation-Adams-Bashforth scheme [45]. In near MFUs, we focus on domain

	Wi	$\delta_x^+$	$\delta_z^+$	$\delta_t$
Growth/overshoot stage	Newt.	3.60	1.80	0.004
	28	3.60	1.80	0.004
	40	4.80	2.74	0.005
	100	4.80	2.74	0.005
ES and turbulent core		8.57	5.11	0.008

Table 1: Numerical details for domain  $L_x^+ \times L_z^+ = 720 \times 230$ . For all the simulations,  $N_y = 145$ ,  $\delta_{y,\min}^+ = 0.025$  and  $\delta_{y,\max}^+ = 2.28$ .

of  $L_x^+ \times L_z^+ = 720 \times 230$ , which is a little larger than but still at the same order of magnitude as an MFU [30, 76]. For dynamics on the ES and in the turbulent core, the numerical resolution in the  $xz$  plane is the same as our previous studies [76, 75, 78, 77, 74]:  $\delta_x^+ = 8.57$  and  $\delta_z^+ = 5.11$ . However, during the initial stage of rapid turbulence growth and overshoot (see fig. 3.1), higher resolution is required:  $\delta_x^+ = 3.60$  and  $\delta_z^+ = 1.80$  are used for the Newtonian and Wi=28 cases;  $\delta_x^+ = 4.80$  and  $\delta_z^+ = 2.74$  are used for Wi=40 and Wi=100 cases. The number of Chebyshev modes  $N_y = 145$  is kept the same for all simulations, which is doubled compared with our previous studies and gives  $\delta_{y,\min}^+ = 0.025$  at the walls and  $\delta_{y,\max}^+ = 2.28$  at the channel center. We have tested multiple resolutions and concluded that the ones reported here (which are much higher than those in regular DNS) are required to fully resolve the small-scale flow structures observed during the transition (see fig. 3.10). Our resolution is also higher than that of the recent numerical studies of the transient transition process [1, 22]. The time step size is chosen with the Courant-Friedrichs-Lewy (CFL) stability condition and varies with resolutions: for the growth/overshoot stage  $\delta_t = 0.004$  is used for the Newtonian and Wi = 28 cases and  $\delta_t = 0.005$  is used for the Wi = 40 and 100 cases; for the ES and turbulent core,  $\delta_t = 0.008$  is used (see table 1).

In extended domains, we tried  $L_x^+ \times L_z^+ = 4000 \times 800$  and  $L_x^+ \times L_z^+ = 8000 \times 800$ ,

	Wi	$\delta_x^+$	$\delta_z^+$	$\delta_t$	$\delta_{y,\min}^+$	$\delta_{y,\max}^+$
ES		33.3	8.89	0.02	0.0809	3.71
Afterwards	Newt.	6.17	6.25	0.005	0.025	2.28
	64	6.17	6.25	0.01	0.025	2.28

Table 2: Numerical details for domain  $L_x^+ \times L_z^+ = 8000 \times 800$ .

finally deciding on the latter one because of the edge tracking result. For dynamics on the ES, the numerical resolution is  $\delta_x^+ = 33.3$ ,  $\delta_z^+ = 8.89$ ,  $\delta_{y,\min}^+ = 0.0809$  and  $\delta_{y,\max}^+ = 3.71$  (the number of Chebyshev modes  $Ny = 73$ ). And the higher resolution is required afterwards:  $\delta_x^+ = 6.17$ ,  $\delta_z^+ = 6.25$ ,  $\delta_{y,\min}^+ = 0.025$  and  $\delta_{y,\max}^+ = 2.28$  (the number of Chebyshev modes  $Ny = 145$ ). The time step size is chosen with the Courant-Friedrichs-Lewy (CFL) stability condition and varies with resolutions: for the growth/overshoot stage  $\delta_t = 0.005$  is used for the Newtonian and  $\delta_t = 0.01$  is used for the  $Wi = 64$ ; for the ES,  $\delta_t = 0.02$  is used (see table 2).

An artificial diffusion term  $1/(\text{ScRe})\nabla^2\boldsymbol{\alpha}$  with  $Sc = 0.5$  is applied to the FENE-P equation for better numerical stability [58], which is the same as our previous studies. The numerical code used in this study is based on the open-source project **Channelflow**, which is a C++ library for Newtonian DNS; the code was extended by Xi [73] for viscoelastic simulation.

## 2.2 Numerical edge tracking

Given a pair of initial states  $\mathbf{X}_T = [\mathbf{v}_T, \boldsymbol{\alpha}_T]$  and  $\mathbf{X}_L = [\mathbf{v}_L, \boldsymbol{\alpha}_L]$  known to bound the turbulent basin and laminar state, respectively, a straight line connecting them in the state space

$$\mathbf{X}_\omega \equiv \omega\mathbf{X}_T + (1 - \omega)\mathbf{X}_L \quad (2.2)$$

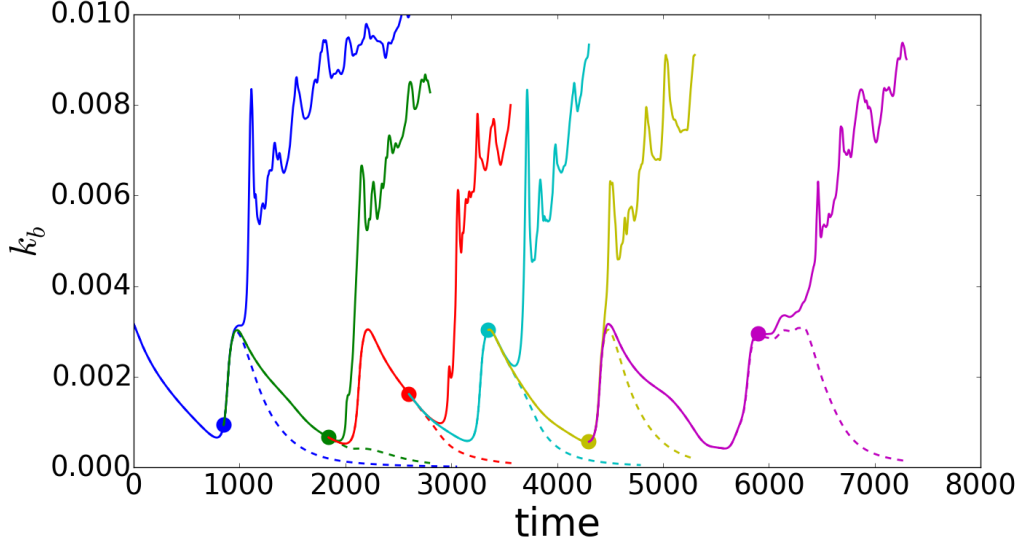


Figure 2.2: Time series of the bulk-averaged TKE of the twin trajectories used in edge tracking ( $Wi = 28$ ). Solid and dashed lines are for trajectories on the turbulent and laminar side, respectively; round dots indicate the points of bisection (see text)

must intersect with the L-T boundary at least once, say, at  $\omega = \omega_e$ . Numerical approximations to the intersection can be found through repeated bisections and DNS shooting tests. A pair of such states is denoted by  $\mathbf{X}_{\omega_e^+}$  and  $\mathbf{X}_{\omega_e^-}$ :  $\omega_e^+(\omega_e^-)$  is infinitesimally larger (smaller) than  $\omega_e$ . Dynamical (DNS) trajectories initiated therefrom,  $\mathbf{X}_{\omega_e^+}(t)$  and  $\mathbf{X}_{\omega_e^-}(t)$ , will travel along the edge for a while before diverging to opposite destinations, effectively pinching and numerically approximating an edge trajectory for a time period. A new round of repeated bisections and shootings are started at the diverging point to further extend the numerical edge solution.

In this study, bisections are carried out to a numerical precision of  $\omega_e^+ - \omega_e^- = 10^{-8}$ . A new round is initiated when the difference in the turbulent kinetic energy (TKE)  $k_b$  between the pinching trajectories grows into the range of  $10^{-6} - 10^{-5}$ , where

$$k \equiv \frac{1}{2}(v_x'^2 + v_y'^2 + v_z'^2), \quad (2.2)$$

(Hereinafter, a prime denotes the fluctuating component, e.g.,  $v'_i \equiv v_i - \langle v_i \rangle$ , and the subscript  $b$  indicates quantities averaged over the bulk, i.e., over the  $x$ ,  $y$  and  $z$  directions.) Time series of  $k_b$  from the edge-tracking process for near MFU case ( $Wi = 28$ ) are shown in fig. 2.2. From an arbitrarily chosen pair of initial states, the  $k_b$  value becomes statistically converged ultimately, indicating that the asymptotic ES has been reached. The method has been developed and widely used in the study of Newtonian turbulence and its transition [60, 56, 54, 12] and numerical details for computing the viscoelastic ES used in this study can be found in Xi and Bai [74].

The initial state used for all DNS shootings in this study corresponds to  $t = 3300$  in fig. 2.2. It is chosen from the bursting phase in the converged edge state trajectory. No additional disturbance is added: we rely on numerical error to trigger the departure from the ES to the turbulent core. Note that by using the same initial state from the  $Wi = 28$  ES for shootings at different  $Wi$ 's, including the Newtonian case, we cannot compare the turbulence growth rates between cases, because except the  $Wi = 28$  case, all other shooting trajectories are subject to an initial disturbance caused by the sudden change in  $Wi$ . However, in all cases, the initial state is close enough to the ES so that the qualitative features of the transition process are preserved. On the other hand, this is the only way to make sure that we are comparing the dynamics initiated from the same state.

The same method for tracking edge state in large domains is applied as  $L_x^+ \times L_z^+ = 720 \times 230$  case. The twin trajectories in edge tracking for  $L_x^+ \times L_z^+ = 8000 \times 800$  are shown in fig. 2.3. Comparing with the near MFU case, flow statistics for ES in the large domain do not vary periodically with time. Instead,  $k_b$  keeps at a steady and pretty low stage within converged ES. We test both  $L_x^+ \times L_z^+ = 4000 \times 800$  and  $L_x^+ \times L_z^+ = 8000 \times 800$  cases, both of whose time series plots show similar evolution in

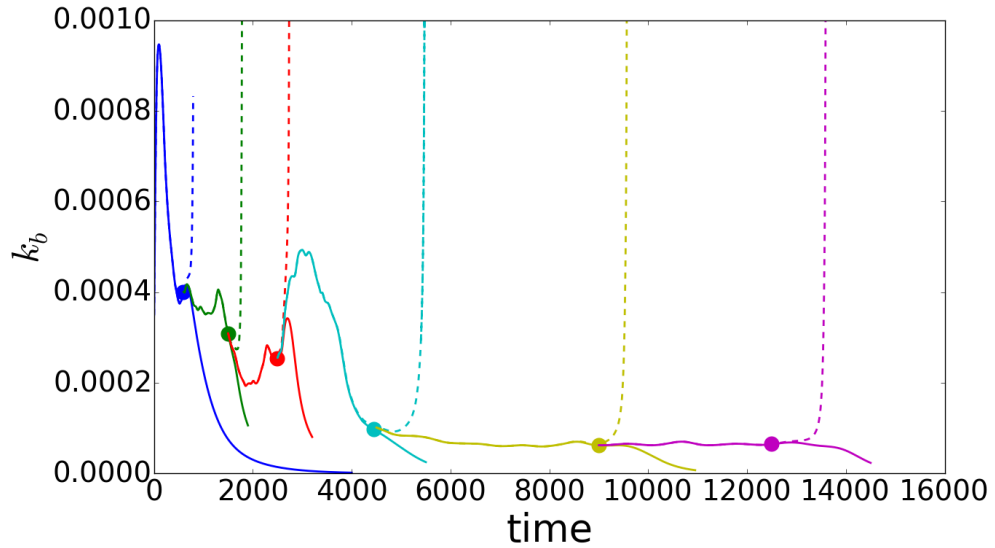


Figure 2.3: Time series of the bulk-averaged TKE of the twin trajectories used in edge tracking (Newtonian,  $L_x^+ \times L_z^+ = 8000 \times 800$ ). Solid and dashed lines are for trajectories on the turbulent and laminar side, respectively; round dots indicate the points of bisection.

edge tracking. However, totally different vortex structures in ES exist for two domain sizes, shown in fig. 2.4, although the  $Q_{\text{rms}}$  are both so close to zero. The  $Q$ -criterion for vortex identification is used [8, 28]. Vortex strength is measured with the scalar field

$$Q \equiv \frac{1}{2} (\| \boldsymbol{\Omega} \|^2 - \| \boldsymbol{\Gamma} \|^2), \quad (2.3)$$

where

$$\boldsymbol{\Omega} \equiv \frac{1}{2} (\nabla \mathbf{v} - \nabla \mathbf{v}^T) \quad (2.3)$$

is the vorticity tensor and

$$\boldsymbol{\Gamma} \equiv \frac{1}{2} (\nabla \mathbf{v} + \nabla \mathbf{v}^T) \quad (2.3)$$

is the rate of strain tensor;  $\| \cdot \|$  represents the Frobenius tensor norm.

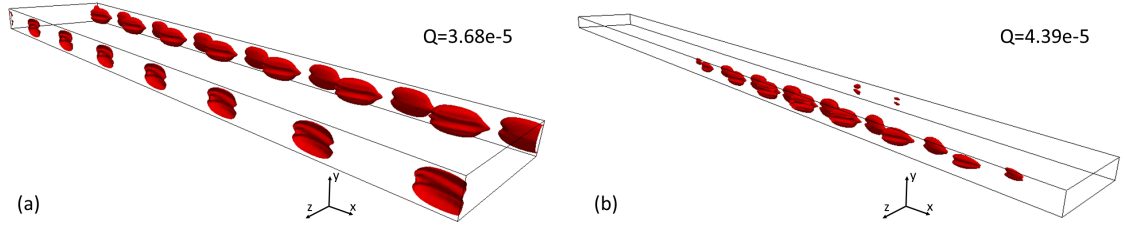


Figure 2.4: Vortex configuration for ES: (a) domain size:  $L_x^+ \times L_z^+ = 4000 \times 800$ ; (b) domain size:  $L_x^+ \times L_z^+ = 8000 \times 800$ . The isosurface of  $Q = Q_{\text{rms}}$  is shown, where  $Q_{\text{rms}}$  is the root mean square of the  $Q$  field.

In a shorter box, pairs of vortex structures are aligned periodically near the centerline of channel, suggesting this box might still be the simple accumulation of smaller boxes. While in  $L_x^+ \times L_z^+ = 8000 \times 800$  box, instead of periodic vortex structures, a strongest localized spot composed of aligned vortex pairs is clearly presented, indicating the essential difference between two domains. This observation is consistent with what Zammert and Eckhardt [81] reported for plane Poiseuille flow. And the difference in flow configuration caused by domain length is also similar with people have observed in plane Couette flow[13, 55]. Undoubtedly, the  $L_x^+ \times L_z^+ = 8000 \times 800$  box is large enough to trigger another mechanism in L-T transition. Thus, we choose the initial state corresponding to  $t = 8900$  in fig. 2.3, a moment within converged ES, for both Newtonian and viscoelastic L-T transient trajectories in extended domain cases.

# Chapter 3

## Results and Discussion

### 3.1 Studies on the near minimal flow unit

#### 3.1.1 Overview

Time series of the Newtonian and  $Wi = 100$  DNS shooting trajectories are shown in fig. 3.1. The process of turbulence growth from the ES is qualitatively similar between the Newtonian and viscoelastic cases. The dynamics stays quiescent for a few hundred time units (TUs) as the system stays close to the ES. A rapid growth stage follows, starting with a sharp increase in the Reynolds shear stress (RSS). (In fig. 3.1, the instantaneous RSS  $-v_x'^* v_y'^*$  is averaged in  $x$  and  $z$ ; the maximum value of the resulting  $y$ -dependent profile, denoted by  $|\langle v_x'^* v_y'^* \rangle|_{\max}$ , is plotted against  $t$ .) In the Newtonian case, the magnitude of  $|\langle v_x'^* v_y'^* \rangle|_{\max}$  at its peak (marked as moment II) is almost 5 times as large as typical magnitudes of the turbulent core. During the same period, a strong overshoot is also observed in TKE but with a slight phase lag of

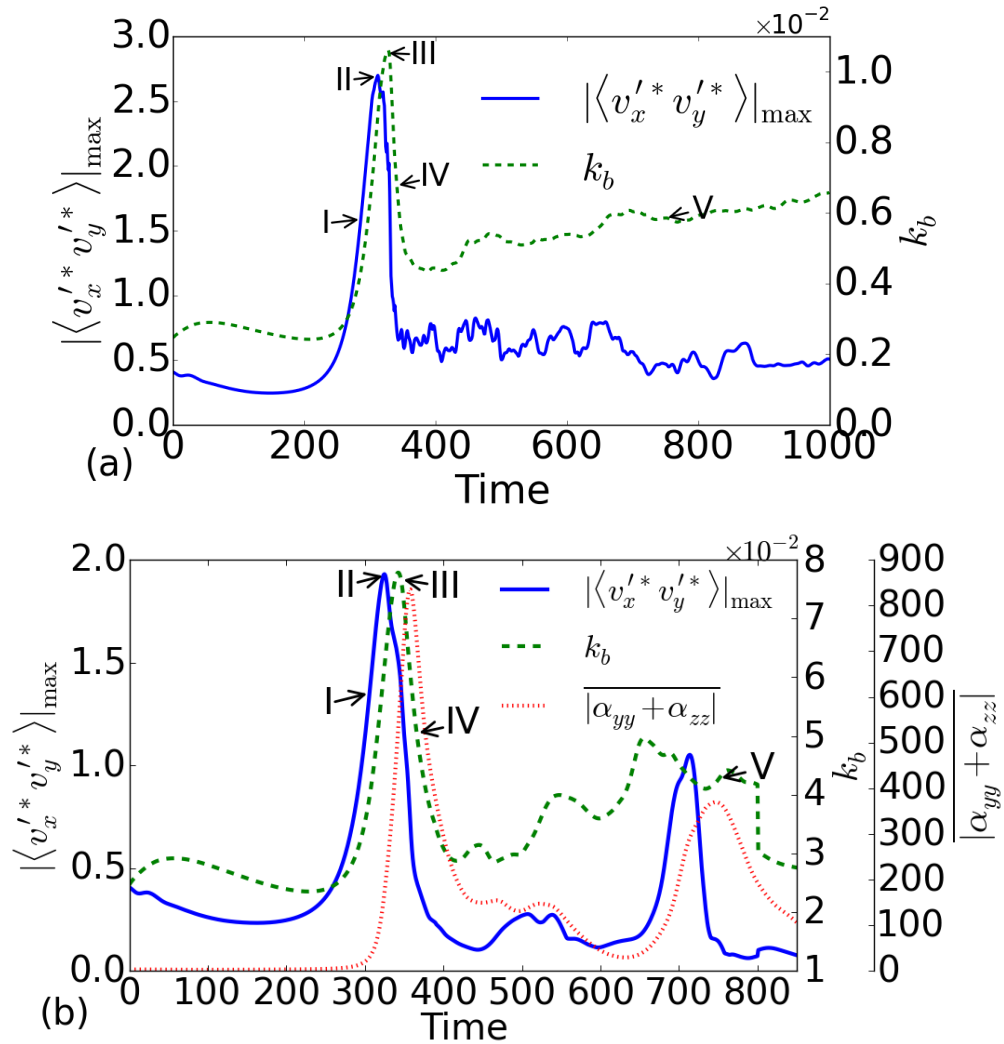


Figure 3.1: Time series of shooting trajectories initiated from the ES: (a) Newtonian; (b)  $Wi = 100$ . The blue solid line (left axis) shows peak values of instantaneous RSS profile; the green dash line (1st right axis) shows bulk-average TKE; the red dotted line (2nd right axis) shows bulk average of  $\alpha_{yy} + \alpha_{zz}$ .

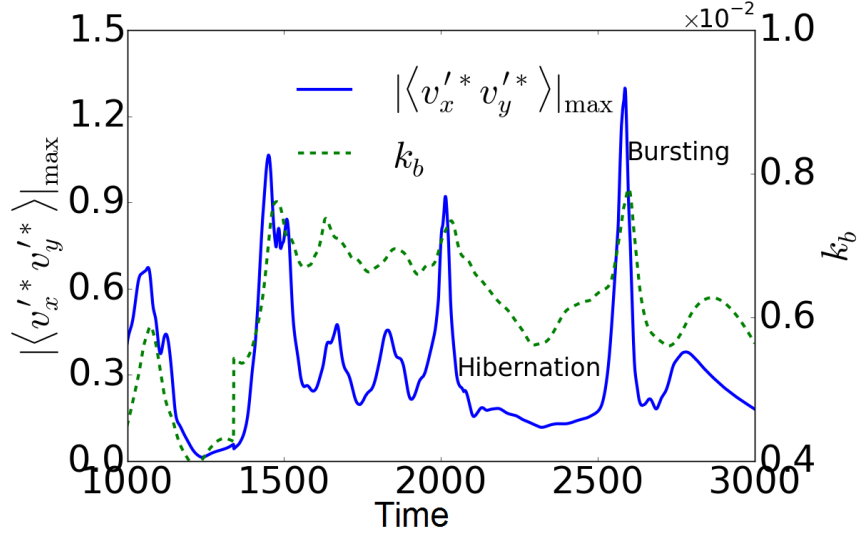


Figure 3.2: Time series of the turbulent core at  $Wi = 40$ : the blue solid line (left axis) shows peak values of instantaneous RSS profiles; the green dash line (right axis) shows bulk-average TKE  $k_b$ .

$\approx 15$  TUs. The peak of TKE is marked as moment III and as we will discuss below, moments II and III have drastically different flow structures. After the overshoots, the RSS quickly drops as the flow enters the turbulent core, where significant differences between the Newtonian and viscoelastic cases start to appear. In particular, the  $Wi = 100$  case is marked by strong intermittency between quiescent periods and turbulent overshoots, corresponding to hibernating and active turbulence. For example, an extended hibernating period can be identified at  $400 \lesssim t \lesssim 650$ , which is followed by a strong overshoot at  $t \sim 700$ . (At  $Wi$  as high as 100, the flow will eventually decay to the laminar state after a few fluctuations in the small simulation domain used here [76, 64]; sustained turbulence is found at  $Wi = 28$  and 40 in this study). Fluctuations in the Newtonian turbulent core are more chaotic. Hibernating turbulence can still occur in the Newtonian limit but at much lower frequency [75, 78]; a small hibernating interval is visible at  $t \sim 900$  in fig. 3.1(a).

fig. 3.2 shows the time series of viscoelastic turbulence in the statistically-converged stage (SCS). A number of hibernating intervals are identified where the RSS takes a deep dive, e.g., at  $t \approx 1200$  and  $2100$ , and each time the flow comes out of hibernation, a strong overshoot is observed. Same as the transient growth in fig. 3.1, the spikes of TKE appear immediately after those of RSS, a direct consequence of the TKE production mechanism (discussed below). Overshoots in RSS, TKE, and wall shear stress were also observed immediately after hibernating intervals in previous studies on the topic [75, 78] and even in earlier Newtonian MFU studies before the term hibernating turbulence was coined. For example, Webber *et al.* [67] noted the intermittent occurrence of the so-called “entropy events” where the TKE drops to very low levels before quickly rising to sharp peaks. The observation here is also consistent with the scenario sketched in fig. 1.1: the flow intermittently breaks the entrapment in the turbulent core (around the UB solutions) and makes visits to the ES; on its return route, it follows the unstable manifold of the ES and experiences a strong spike in turbulent activities, before decaying back to the turbulent core. Jiménez *et al.* [31] argued that the turbulent dynamics cannot be completely described by invariant solutions (both UB and LB ones) and strong and the quick “bursting” event, which corresponds to spikes observed here and is likely transient in nature, is an essential component. In light of this, the earlier framework of active-hibernating transition [75, 78, 20] should now be adjust to a three-stage cycle consisting of the turbulent core (UB), hibernation (ES), and bursting. Since polymer-induced elasticity is known to shorten the time spent at the turbulent core and increase the turnover frequency of these intermittent cycles [75, 78], understanding how polymers affect the bursting dynamics will be essential for a full picture of turbulence approaching MDR. The approach of this study allows us to overcome the difficulty of tracking the intermittent bursting events and directly compare the bursting dynamics between Newtonian and viscoelastic cases.

State space trajectories of different solution objects are projected onto the  $|\langle v_x^* v_y^* \rangle|_{\max} - A_{25}^*$  plane in Figure 3.3, where  $A_{25}^*$  is the value of

$$A^* \equiv y^* \frac{\partial U_m^*}{\partial y^*} \quad (3.2)$$

measured at  $y^* = 25$ . Note that (3.2) comes from taking the differentials of both sides of the log-law relationship of the mean velocity

$$U_m^* = A^* \ln y^* + B^* \quad (3.2)$$

and  $A^*$  defined in (3.2) is thus interpreted as the local log-law slope. Intermittency in near-wall coherent structures was found to be instantly reflected in changes in  $A^*$  [78, 74]. Transient solutions of Newtonian and three viscoelastic cases, initiated from the same point on the edge state, all move along the ES for a segment before deviation, which is expected for dynamics near a saddle point. After the departure, the RSS quickly rises but the decline in  $A_{25}^*$  is slow, while different trajectories remain close to one another. Separation between the trajectories only occurs as the RSS reaches its peak, after which the drop of  $A_{25}^*$  accelerates as the trajectories spiral into the regions corresponding to their respective turbulent cores. Interestingly, for all four cases tested, the point where the trajectory turns its direction (to the left) and the mean velocity starts to significantly drop is close to Virk MDR magnitude  $A_{25}^* = A_{\text{Virk}} = 11.7$ , which will be further discussed below. With increasing  $Wi$ , the RSS magnitude at the top of the overshoot decreases (as expected); the turbulent core also shifts towards the lower right direction, reflecting the lower friction drag. Intermittent excursion towards the direction of the ES is observed within the turbulent core, which corresponds to hibernating turbulence and becomes more frequent at

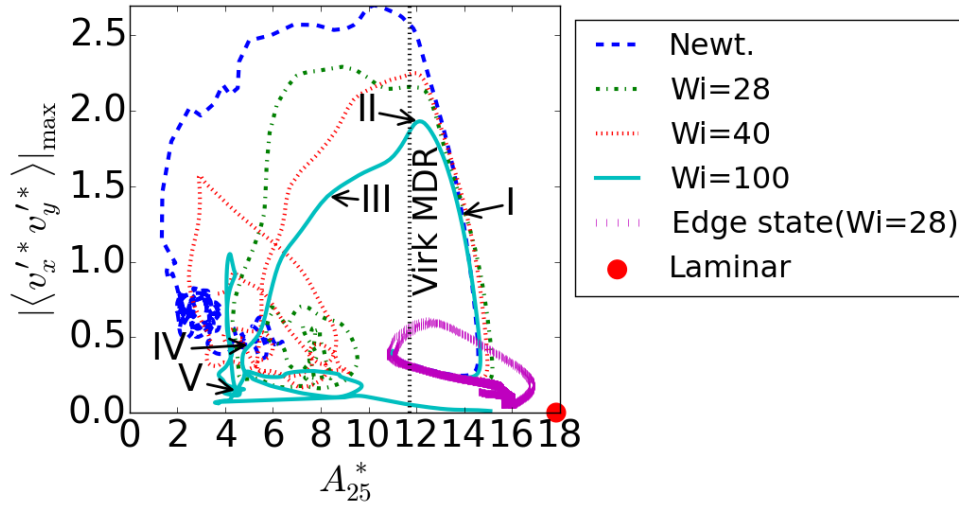


Figure 3.3: State-space projection of solution trajectories. Moments I~IV on the  $Wi = 100$  trajectory are labeled in fig. 3.1(b).

higher  $Wi$ . Similarities between hibernating turbulence and the ES were extensively discussed in previous studies [77, 74]. Overall, the state-space topology observed here is consistent with the schematic sketch of fig. 1.1.

The initial close alignment between trajectories of different  $Wi$  indicates that at least during the early stage of turbulence development the impact of polymers is limited. Time series of  $\alpha_{yy} + \alpha_{zz}$ , which measures the polymer extension in the  $y - z$  plane, is shown in fig. 3.1(b). Although polymer extension in the three-dimensional space is measured by

$$\text{tr}(\boldsymbol{\alpha}) \equiv \alpha_{xx} + \alpha_{yy} + \alpha_{zz}, \quad (3.3)$$

previous studies [77, 78] have shown that, even without turbulent motions, substantial polymer stretching is caused by the mean shear of the flow, resulting in a large  $\alpha_{xx}$  contribution to  $\text{tr}(\boldsymbol{\alpha})$ . Turbulence-induced polymer extension is more clearly observed when only the  $\alpha_{yy}$  and  $\alpha_{zz}$  components are considered. The magnitude of  $\alpha_{yy} + \alpha_{zz}$  increases sharply during the overshoot but only as a reaction to the surge in

turbulent intensity: the peak of  $\alpha_{yy} + \alpha_{zz}$  comes  $\approx 15$  TUs later than moment III. The implication of this observation is twofold. First, polymer dynamics does not drive the instability, and turbulence is still initiated in a similar manner as Newtonian flow. Second, as the trajectory leaves the ES in the state space, it travels through a region with minimal polymer-turbulence interaction before polymer effects become significant. The latter point is consistent with our earlier speculation that in addition to the ES, there is a group of states insensitive to polymer additives (see fig. 1.1) located in its neighborhood. These states, or a part thereof, are likely to dominate the universal and self-sustaining turbulent activities at MDR.

### 3.1.2 Mean velocity development and shear stress balance

Mean velocity profiles of turbulence at its SCS are shown in fig. 3.4(a) which gradually increase from the Prandtl-von Kármán (PvK) log law of Newtonian turbulence [33]

$$U_m^+ = 2.5y^+ + 5.5 \quad (3.4)$$

to the Virk log law of MDR ((1.0)); all profiles overlap with the viscous sublayer asymptote at  $y^+ \lesssim 5$

$$U_m^+ = y^+ \quad (3.4)$$

as they should [46]. At  $Wi = 100$ , turbulence does not sustain in the current domain size; therefore the average is taken between  $900 \leq t \leq 1100$ , before relaminarization starts. Instantaneous mean velocity profiles at this  $Wi$  during the transient development stage are shown in fig. 3.4(b).

As the departure from the ES starts, the slope of the profile rises above that of the

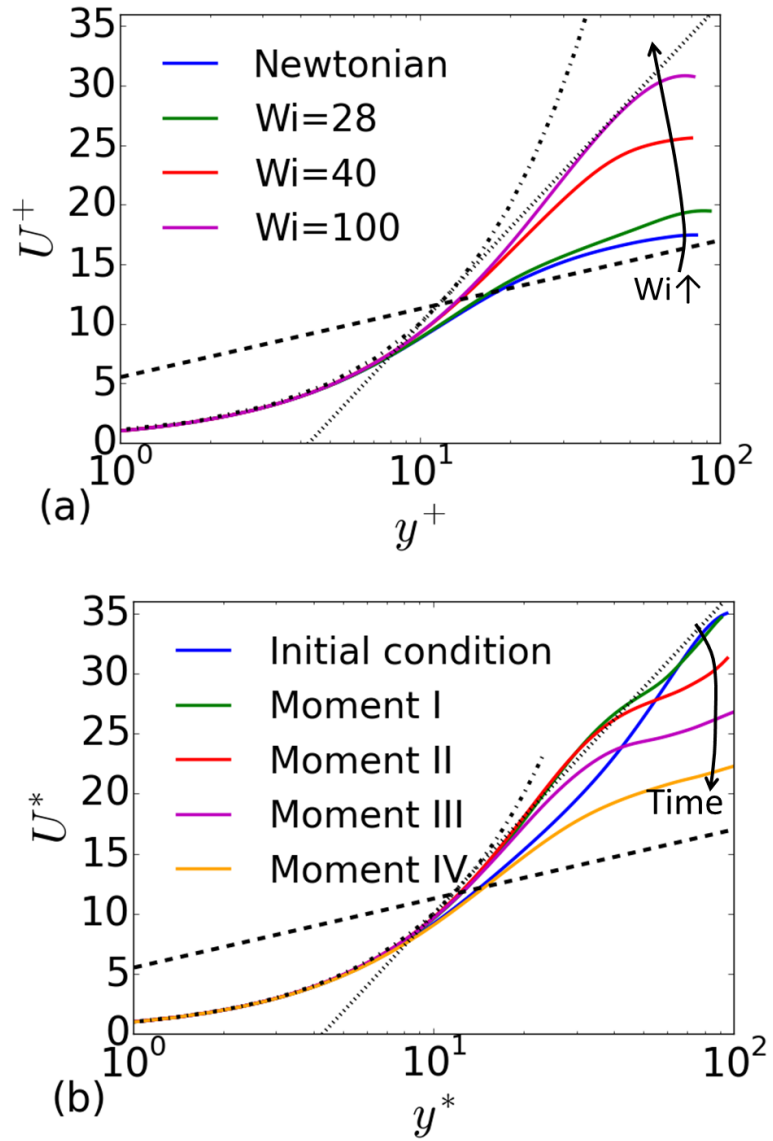


Figure 3.4: Mean velocity profiles: (a) time-average profiles for Newtonian and viscoelastic cases (at the SCS); (b) instantaneous profiles for initial condition and moments I–IV (as labeled in fig. 3.1;  $Wi = 100$ ) during the transient development (dot-dashed: viscous sublayer; dashed: PvK log law; dotted: Virk log law).

Virk log law while the reduction of  $U_m$  starts near the channel center (moment I). As time moves forward, this deficit extends into the near-wall layer as the profile drops towards the PvK log law.

As mentioned earlier, the log-law slope of the profile, at least in the near-wall layer, crosses the magnitude of  $A_{\text{Virk}} = 11.7$  near moment II when the state-space trajectory takes a sharp turn in fig. 3.3. The Reynolds equation, which governs the development of the mean velocity  $U_m \equiv \langle v_x \rangle$ , is obtained by taking the  $x$ -component of (2.1), applying the Reynolds decomposition to all dependent variables, and taking the ensemble average on both sides. The resulting equation (cast in inner scales where stress and pressure are scaled with  $\tau_w$  and time with  $\eta/\tau_w$ )

$$\frac{\partial U_m^+}{\partial t^+} = \frac{\partial \langle \tau_{xy}^+ \rangle}{\partial y^+} - \frac{d \langle p^+ \rangle}{dx^+} \quad (3.4)$$

shows that the change of  $U_m$  is determined by the streamwise mean pressure gradient and the wall-normal gradient of the mean shear stress

$$\langle \tau_{xy}^+ \rangle \equiv \beta \frac{\partial U_m^+}{\partial y^+} + \langle -v_x'^+ v_y'^+ \rangle + \frac{1 - \beta}{\text{Wi}} \langle \tau_{p,xy} \rangle. \quad (3.4)$$

Recall the definition in (3.2): the log-law slope is directly determined by the mean velocity gradient  $\partial U_m^+ / \partial y^+$  (we use the +-units here instead of the \*-units to avoid the complexity of changing scaling between different instants; this choice does not qualitatively affect any following discussion), whose evolution is governed by

$$\begin{aligned} \frac{\partial}{\partial t^+} \left( \frac{\partial U_m^+}{\partial y^+} \right) &= \beta \frac{\partial^3 U_m^+}{\partial (y^+)^3} + \frac{\partial^2}{\partial (y^+)^2} \langle -v_x'^+ v_y'^+ \rangle \\ &+ \left( \frac{1 - \beta}{\text{Wi}} \right) \frac{\partial^2 \langle \tau_{p,xy} \rangle}{\partial (y^+)^2}. \end{aligned} \quad (3.5)$$

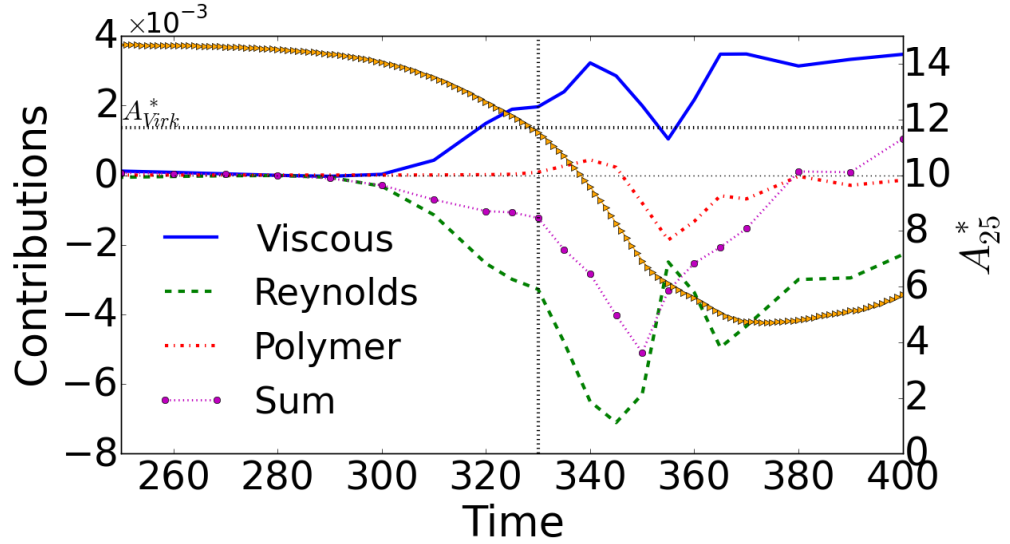


Figure 3.5: Contributions to the mean velocity gradient development according to (3.5) (left) and the log-law slope  $A_{25}^*$  (right) for  $Wi = 100$ . Horizontal reference lines are added at the 0 mark of the left axis and the  $A_{\text{text}} = 11.7$  mark of the right axis; the vertical reference line marks the moment when  $A_{25}^* = A_{\text{Virk}}$ . Time axis matches that of fig. 3.1.

(3.5) is obtained by taking the  $y^+$  derivative of both sides of (3.4) and noting that  $d\langle p^+ \rangle / dx^+$  is constant. The three terms on the right-hand side (RHS) describe the contributions from viscous, Reynolds, and polymer shear stress, respectively. Time series of these terms are shown in fig. 3.5 for the transient development period in fig. 3.1(b). All terms start at zero until the RSS term first deviates and acts to bend down the  $U_m$  profile. The decline of  $A_{25}^*$  is initially slow but it speeds up and crosses the  $A_{\text{Virk}}$  level at  $t = 330$ , which is near moment II ( $t = 325$ ). Exactly at this crossover point, the RSS term takes a sharp turn downwards, leading to the rapid decay of  $A_{25}^*$  and the turn of trajectories in fig. 3.3. We have examined the Newtonian case and other  $Wi$  and the coincidence between  $A_{25}^* = A_{\text{Virk}}$  and the turn of the RSS contribution is observed in all cases. This seems to suggest that  $A_{\text{Virk}} = 11.7$  corresponds to a critical magnitude below which the RSS can quickly drag the mean flow towards the PvK asymptote. Unraveling the connection between  $A_{25}^*$  and the

RSS profile will thus reveal the quantitative origin of the Virk asymptote. It is also consistent with the overall framework and earlier hypothesis that MDR corresponds to one or more intrinsically Newtonian flow states that polymers only help to expose, which – although are not located on the ES – are closely associated with the dynamics in its neighborhood. Much caution, however, needs to be taken before any conclusions can be drawn. So far we only have data for one Re and one domain size: any theory for the Virk asymptote must withstand verification at a wide range of Re. Further research is still needed. Finally, the polymer shear stress (PSS) term stays close to zero until around moment III ( $t = 345$ ), after the significant deviations in other terms. This again supports the conclusion that polymers act in reaction to the growth of instability and do not have substantial impact until full-fledged turbulence has developed.

Instantaneous profiles of the viscous shear stress (VSS), RSS, and PSS – the three contributions to the total shear stress (TSS) defined in (3.4) – of representative moments are plotted in figs. 3.6 and 3.7. The steady-state solution to (3.4) is

$$\tau_{xy}^+ = 1 - \frac{y^+}{\sqrt{2\text{Re}}} \quad (3.7)$$

which is shown as a reference line in all panels. The initial state fig. 3.7(a), taken from the ES, has a moderate RSS and the VSS is sizeable across the channel; the PSS is negligible at the ES. (Since the ES solution is asymmetric [77, 74] with respect to the center plane and so is the transient trajectory initiated thereat, only the half channel with stronger turbulent activity is shown in figs. 3.6 and 3.7.) Evolution of the RSS and VSS is qualitatively similar between the Newtonian and viscoelastic cases. As turbulence starts to develop, the RSS quickly increases and reaches its maximum at moment II, which is much higher than the magnitude of the steady-state TSS. The profile also takes a sharper form, resulting in a large (negative) second-order derivative

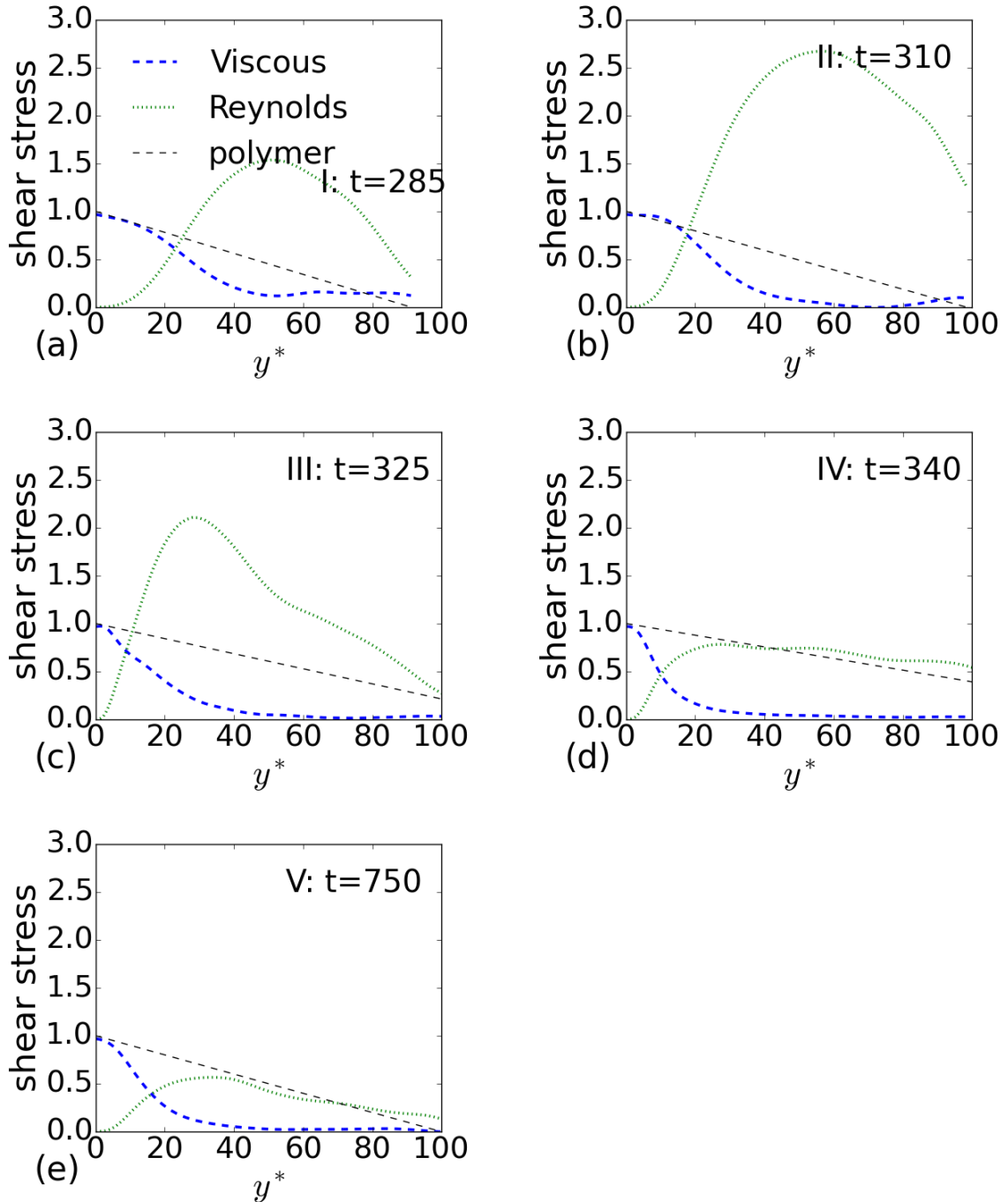


Figure 3.6: Contributions to the total shear stress in the Newtonian case: (a)~(e) – moments I~V; black dot-dashed line is the steady-state TSS ((3.7)).

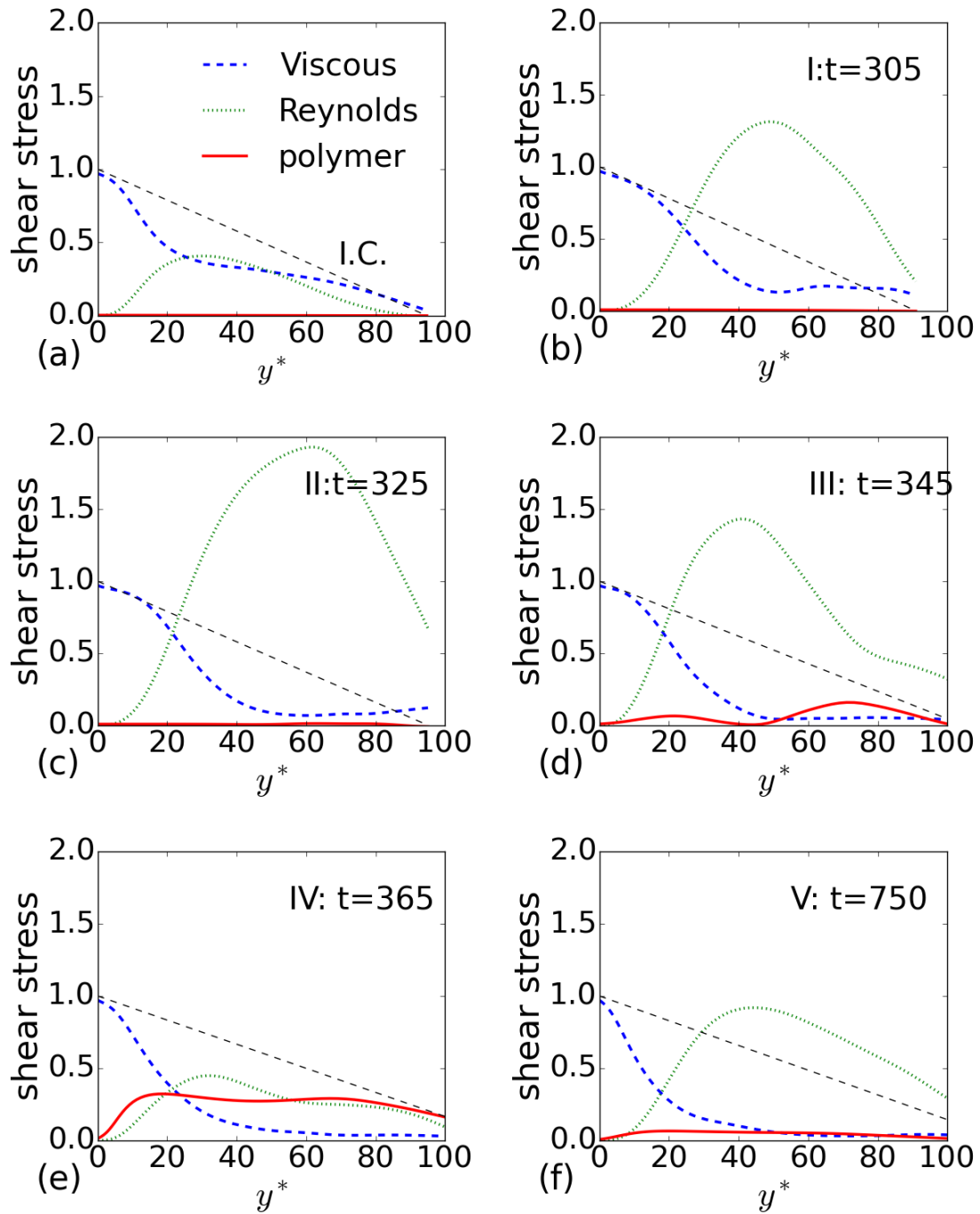


Figure 3.7: Contributions to the total shear stress in the  $Wi = 100$  case: (a) initial condition; (b)~(f) – moments I~V; black dot-dashed line is the steady-state TSS ((3.7)).

that quickly suppresses in the mean velocity gradient, as discussed in fig. 3.5. The RSS starts to decay at moment III. At moments IV and V, its shape resembles the typical form in steady-state turbulence which peaks in the buffer layer. The VSS, meanwhile, has retreated to the near-wall region only. For the viscoelastic case, the PSS remains small until moment III, where its magnitude becomes comparable with that of the RSS.

The role of PSS at MDR is an issue often debated. Warholic *et al.* [65] has measured a nearly vanishing magnitude of RSS at MDR. Although the PSS cannot be measured directly in experiments, it was inferred from the TSS magnitude ((3.7)) that the PSS has filled in the deficit left by the RSS. It was thus argued that MDR is a state in which the mechanism of sustaining turbulence in Newtonian flow has been replaced by a polymer-dominated instability. However, other studies (experimental and numerical) showed that the RSS does not necessarily vanish and is not always overpassed by the PSS at MDR [48, 36, 39]. This complexity can be explained now considering the dynamical cycle of turbulent core – hibernation – bursting depicted in fig. 1.1. Based on fig. 3.7, large PSS only occurs during the bursting stage and depending on the relative time spent in different stages, the time-averaged shear stress profiles may or may not show a PSS larger than the RSS. As discussed below, even at moment III where the PSS is the highest, polymers still plays a suppressing role on turbulence: high PSS does not indicates an elastic instability at MDR.

### 3.1.3 Flow structure development

Streamwise velocity in the  $x - z$  plane at  $y^+ = 24.85$  is shown in figs. 3.8 and 3.9. The initial moment at the ES (fig. 3.9(a)) shows one pair of low- and high-speed

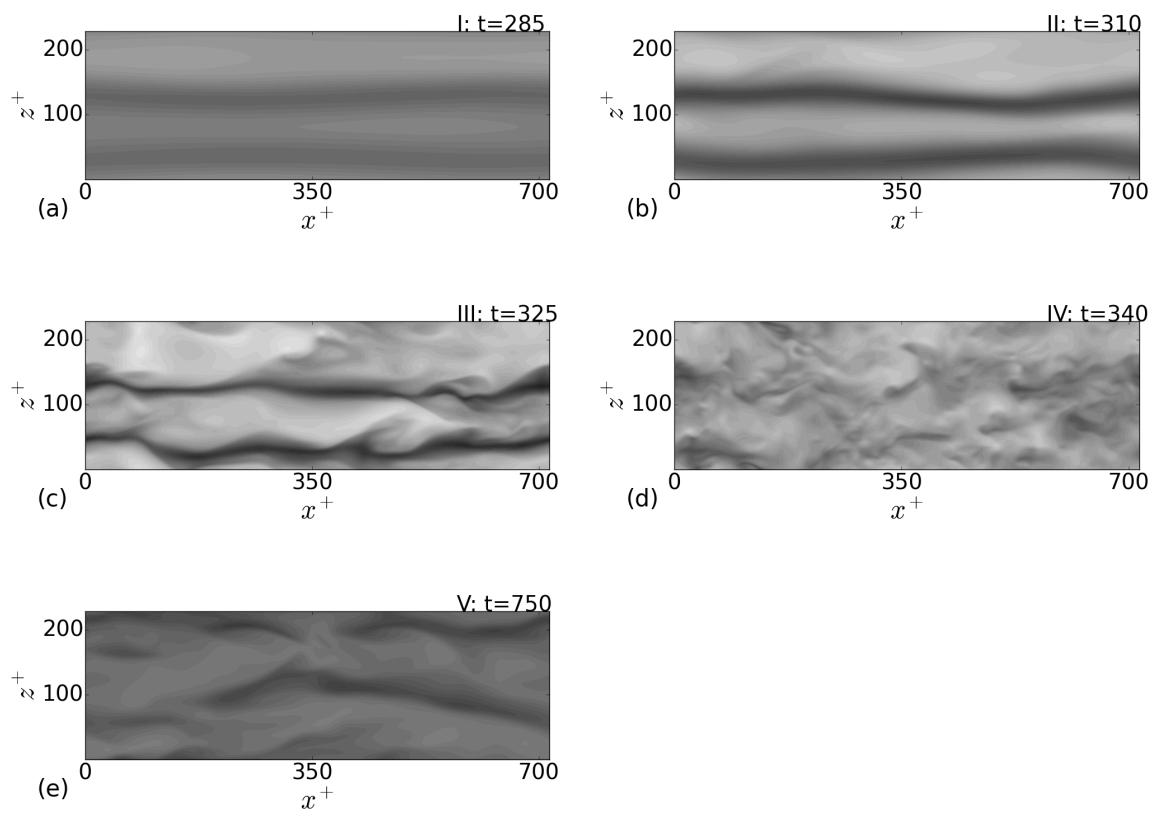


Figure 3.8: Streamwise velocity distribution at  $y^+ = 24.85$  for the Newtonian case: (a)~(e) – Moments I~V; the color ranges from black to white for 0 to 1.

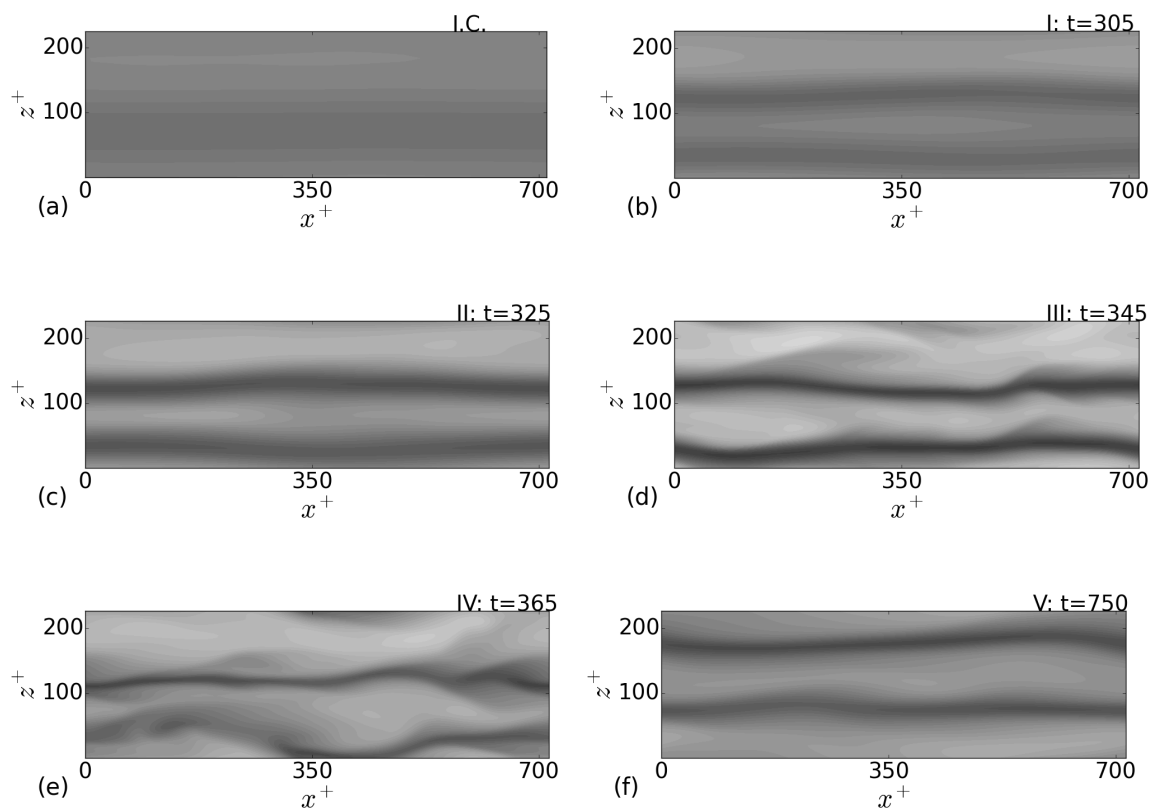


Figure 3.9: Streamwise velocity distribution at  $y^+ = 24.85$  for the  $Wi = 100$  case: (a) initial condition; (b)~(f) Moments I~V; the color ranges from black to white for 0 to 1.

streaks in the domain. The streaks are weak in magnitude, showing a small velocity variation compared to the range of the color map, and straight in shape. For both Newtonian and viscoelastic cases, as instability starts to develop (moment I), the low-speed streak splits into two. The streaks further intensify as the RSS increases up to its peak magnitude at moment II, where streamwise variation becomes clearly visible. Observations between the Newtonian and viscoelastic cases start to differ at moment III. In the former (fig. 3.8(c)), streak instability quickly breaks down the structure, leading to a domain filled by small-scale structures and strong velocity fluctuations as it leaves the bursting stage. These fluctuations reorganize into weak streaks as the flow enters the turbulent core (moment V; fig. 3.8(e)). By contrast, at high  $Wi$ , this breakdown into high-intensity fluctuations is largely avoided and the streaky structure persists through moments III and IV.

Vortex configuration for the same moments are shown in figs. 3.10 and 3.11. The initial moment from the ES shows weak ( $Q_{\text{rms}} = 0.000237$ ) vortices, which are mostly straight along the streamwise direction and localized at one side of the channel. Asymmetry and structural localization is typical of the ES in Poiseuille flow [74]. The growth of instability during the rise of the RSS is similar between the Newtonian and viscoelastic cases, where the streak intensification (figs. 3.8 and 3.9) is accompanied by the strengthening of the vortices:  $Q_{\text{rms}}$  increases to 0.0161 at moment I and 0.181 at moment II for the Newtonian case. Meanwhile the vortices spread to most of the channel and their shape becomes distorted in all three dimensions, which is also reflected in the streak waviness observed in figs. 3.8 and 3.9. For the Newtonian case, the streak breakdown corresponds to an abrupt change in the vortex configuration. Within the 15 TUs between moments II and III,  $Q_{\text{rms}}$  jumps from 0.181 to 1.23 and

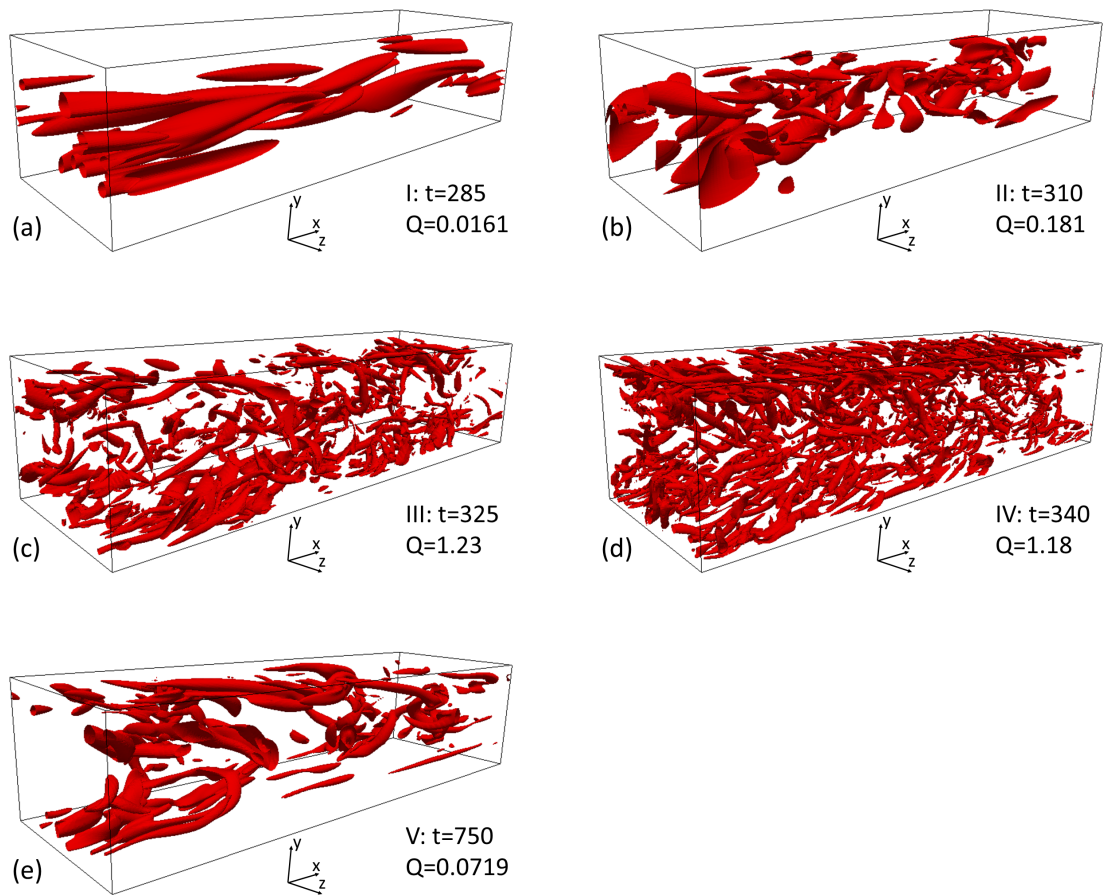


Figure 3.10: Vortex configuration for the Newtonian case: (a)–(e) are moments I–V; the isosurface of  $Q = Q_{\text{rms}}$  is shown, where  $Q_{\text{rms}}$  is the root mean square of the  $Q$  field.

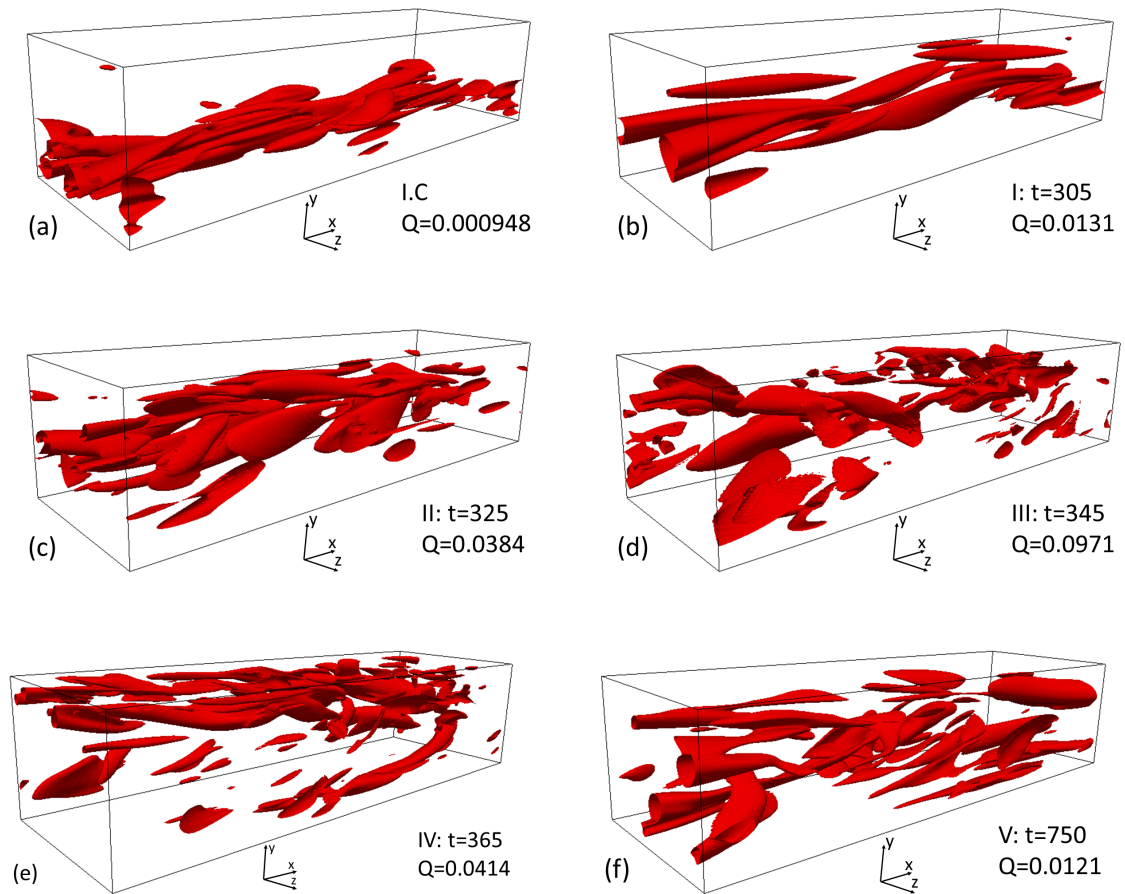


Figure 3.11: Vortex configuration for the  $Wi = 100$  case: (a) initial conditions and (b)–(f) are moments I–V; the isosurface of  $Q = Q_{\text{rms}}$  is shown (in (a)  $Q = 4.0Q_{\text{rms}}$ ), where  $Q_{\text{rms}}$  is the root mean square of the  $Q$  field.

a limited number of relatively large vortices at moment II suddenly blows up into numerous small-scale but high-intensity vortices filling the entire domain. Our finding resonates with the observation by Webber *et al.* [67] of the temporally intermittent bursting events in a MFU, which they called “entropy events”: during these events, TKE is initially distributed over very few flow modes as its magnitude quickly rises; then within a very short period of time, TKE is suddenly redistributed to a broad spectrum of scales. This again confirms that the bursting events come from the trajectories that closely follow the unstable manifold of the ES to a strong overshoot in TKE (fig. 1.1), which happens after close visits to the ES (hibernating turbulence). At high  $Wi$ , this sudden breakdown at moment III (fig. 3.11(d)) is largely avoided and vortices evolve continuously into their turbulent-core configuration. This, together with the observations in , points to the same scenario for the role of polymers on the development of turbulence as well as on bursting events: polymers do not noticeably change the initial growth of instability, which mainly involves the intensification of streaks and distortion of vortical structures; however, after the RSS has reached its peak, polymers stabilize the primary large-scale vortices from breaking down.

### 3.1.4 Turbulence growth and polymer effects

The growth of turbulence as it departs from the ES and the polymer effects thereon are now quantitatively analyzed through the budgets of the TKE and Reynolds stress, which can be derived from the equation of motion (2.1) following the example of Newtonian flow. The evolution of TKE is

$$\frac{\partial k}{\partial t} + \langle \mathbf{v} \rangle \cdot \nabla k + \nabla \cdot \mathbf{T}^k = \mathcal{P}^k - \epsilon_v^k - \epsilon_p^k, \quad (3.11)$$

where

$$\mathcal{P}^k \equiv -\nabla \langle \mathbf{v} \rangle : \langle \mathbf{v}' \mathbf{v}' \rangle = -\langle v'_x v'_y \rangle \frac{d\langle v_x \rangle}{dy} \quad (3.11)$$

is the production of TKE (the second equality holds because  $d\langle v_x \rangle/dy$  is the only non-zero component of  $\nabla \langle \mathbf{v} \rangle$ ),

$$\epsilon_v^k \equiv \frac{2\beta}{\text{Re}} \langle \mathbf{\Gamma}' : \mathbf{\Gamma}' \rangle \quad (3.11)$$

and

$$\epsilon_p^k \equiv \frac{2(1-\beta)}{\text{ReWi}} \langle \boldsymbol{\tau}'_p : \mathbf{\Gamma}' \rangle \quad (3.11)$$

are the consumption rates of TKE by viscous dissipation and by conversion into elastic energy, respectively ( $\mathbf{\Gamma}'$  and  $\boldsymbol{\tau}'_p$  are the fluctuating components of the rate of strain ((2.3)) and polymer stress tensors), and  $\mathbf{T}_k$  groups all terms contributing to the flux of  $k$  transport, which only moves the TKE spatially but does not convert it to other forms; it therefore will not be further discussed in this study.

The production of the TKE is the product of the RSS  $-\langle v'_x v'_y \rangle$  and the mean shear rate  $d\langle v_x \rangle/dy$ , which explains why the surge in the RSS during the turbulence growth process is followed by a strong spike in the TKE. Evolution of the RSS is governed by

$$\begin{aligned} \frac{\partial \langle -v'_x v'_y \rangle}{\partial t} + \langle \mathbf{v} \rangle \cdot \nabla \langle -v'_x v'_y \rangle + \nabla \cdot \mathbf{T}^R = \\ \mathcal{P}^R + \mathcal{R}^R - \epsilon_v^R - \epsilon_p^R \end{aligned} \quad (3.11)$$

where

$$\mathcal{P}^R \equiv \langle v'_y v'_y \rangle \frac{d\langle v_x \rangle}{dy} \quad (3.11)$$

$$\mathcal{R}^R \equiv - \left\langle p' \left( \frac{\partial v'_x}{\partial y} + \frac{\partial v'_y}{\partial x} \right) \right\rangle \quad (3.11)$$

$$\epsilon_v^R \equiv - \frac{2\beta}{\text{Re}} \sum_{w=x,y,z} \left( \left\langle \Gamma'_{xw} \frac{\partial v'_y}{\partial w} \right\rangle + \left\langle \Gamma'_{yw} \frac{\partial v'_x}{\partial w} \right\rangle \right) \quad (3.11)$$

$$\epsilon_p^R \equiv - \frac{2(1-\beta)}{\text{ReWi}} \sum_{w=x,y,z} \left( \left\langle \tau'_{p,xw} \frac{\partial v'_y}{\partial w} \right\rangle + \left\langle \tau'_{p,yw} \frac{\partial v'_x}{\partial w} \right\rangle \right) \quad (3.11)$$

are the production, pressure-rate-of-strain, viscous conversion, and elastic conversion terms, respectively;  $\mathbf{T}^R$  again is the flux of RSS not discussed here. According to (3.11), at a given mean shear rate, the RSS is generated by wall-normal velocity fluctuations. In the near wall region they are primarily found between streamwise vortices where velocity streaks are formed by the upward lifting and downward flushing fluid motions. Therefore the rise of the RSS from the ES to moment II is accompanied by the intensification of the streak structures (figs. 3.9 and 3.11).

Figures 3.12 and 3.13 show the TKE and RSS budgets for typical moments of the Newtonian and  $\text{Wi} = 100$  cases. The process is qualitatively similar between the two cases during the surge of the RSS (up to moment II), where the production terms dominate both the budgets of quantities. The RSS production  $\mathcal{P}^R$  has a flatter shape and is larger at around  $y^+ = 40$ , the location of the primary streaks and vortices at the ES (see fig. 3.11(a) and [74]), than in the buffer layer; whereas the TKE production  $\mathcal{P}^k$  peaks in the buffer layer – at  $y^+ \approx 25$ . Between moments II and III, the profiles suddenly change and polymer effects become significant. In the Newtonian

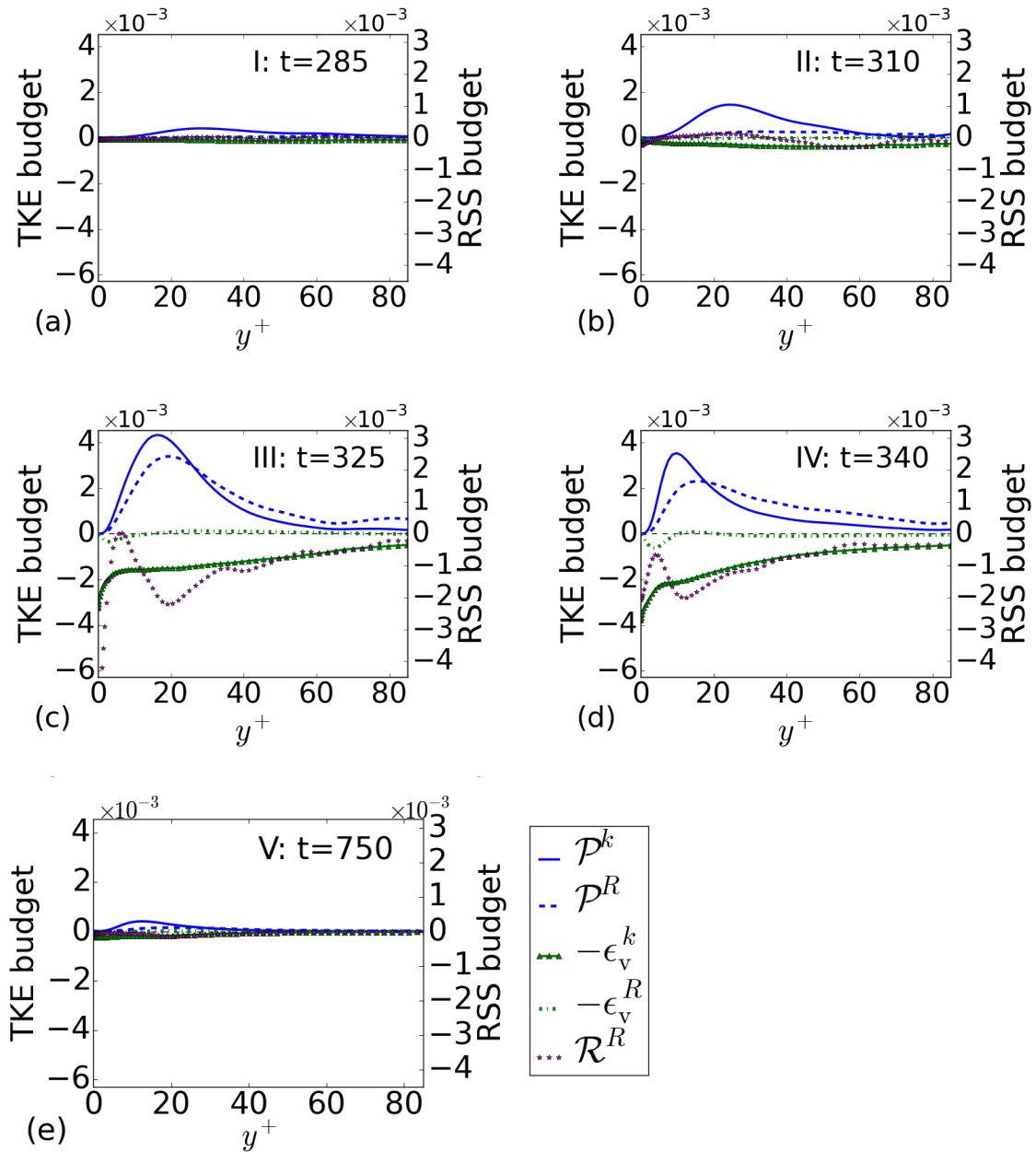


Figure 3.12: TKE and RSS budgets for the Newtonian case: (a)–(e) are moments I–V.

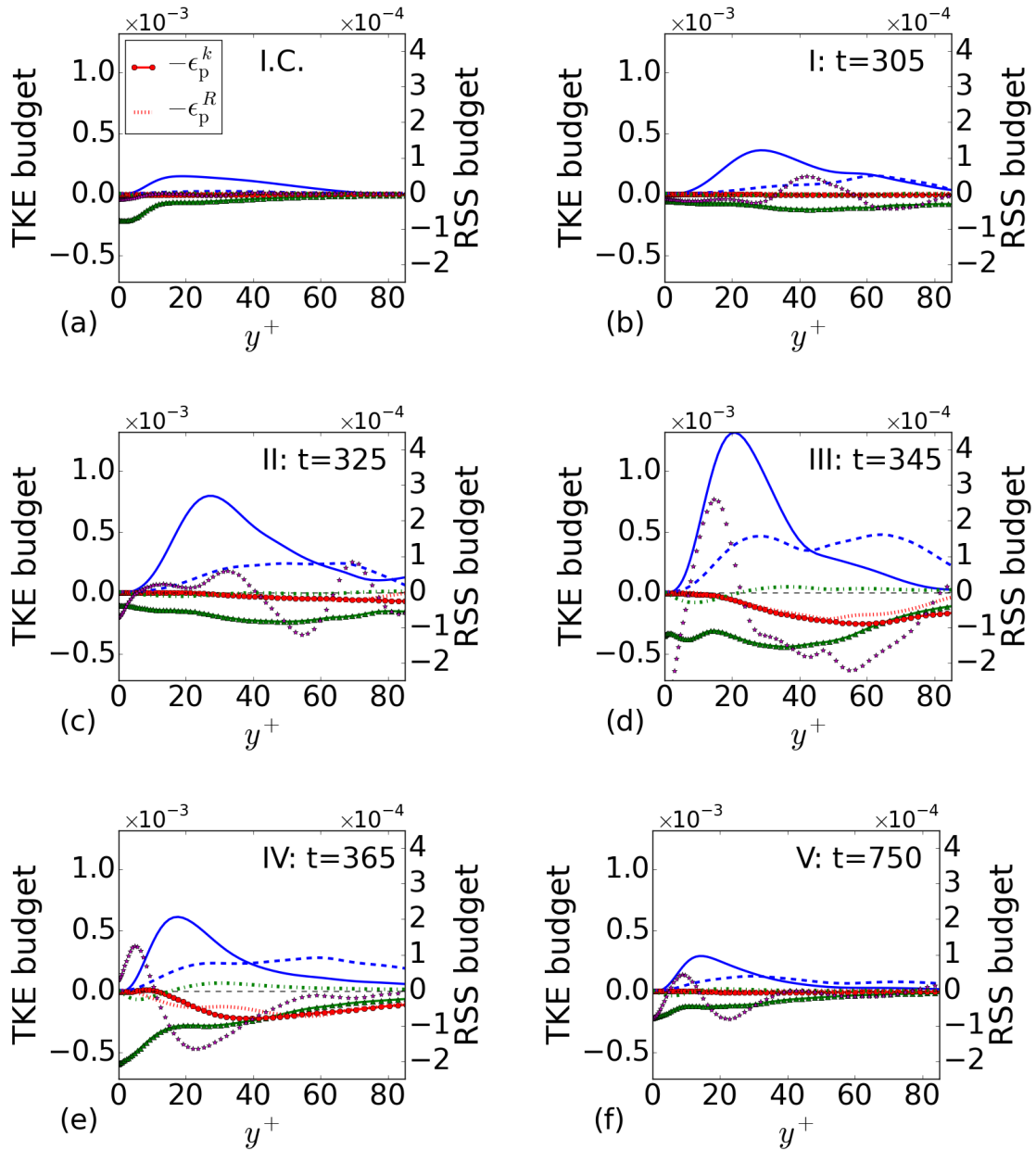


Figure 3.13: TKE and RSS budgets for the  $Wi = 100$  case: (a) initial condition; (b)–(f) are are moments I–V.

case, magnitudes of both  $\mathcal{P}^k$  and  $\mathcal{P}^R$  sharply increase. In addition,  $\mathcal{P}^R$  now peaks in the buffer layer as well and its profile conforms to that of  $\mathcal{P}^k$ , indicating that the high-intensity small-scale flow structures resulting from the breakdown of primary vortices reinforce the RSS generation (which thus completes a positive feedback loop as the RSS further drives the TKE production). The TKE viscous dissipation  $\epsilon_v^k$  also suddenly jumps to a comparable magnitude as that of  $\mathcal{P}^k$ , which eventually tames the fluctuations and regulates the eddies into the typical coherent structures of the turbulent core. For the RSS budget,  $\epsilon_v^R$  is small and  $\mathcal{P}^R$  is counteracted instead by  $\mathcal{R}^R$ . At high Wi, the  $\mathcal{P}^k$  profile at moment III is still similar in shape as the Newtonian case but its magnitude is much lower and the peak location is farther away from the wall. By contrast, because the streak breakdown is now bypassed,  $\mathcal{P}^R$  maintains its flat profile through moment III. Excessive dissipation  $\epsilon_v^k$  near the wall, observed in the Newtonian case at moment III, is also avoided. The polymer elastic conversion terms  $\epsilon_p^k$  and  $\epsilon_p^R$  are trivial until moment III, where their magnitudes suddenly surge and for the TKE budget,  $\epsilon_p^k$  becomes comparable to the viscous term  $\epsilon_v^k$ . In the case of the RSS budget, owing to a combination of lower  $\mathcal{P}^R$  and the additional contribution of  $\epsilon_p^R$ , the  $\mathcal{R}^R$  profile emerges above zero in certain regions. Finally, it is important to note that both  $-\epsilon_p^k$  and  $-\epsilon_p^R$  are always negative, indicating that polymers suppress turbulence throughout the transition or bursting process and there is no evidence for elasticity-driven instability.

### 3.1.5 Initial condition dependence

An important distinction between this study and previous research on bypass transition is that instead of perturbing the laminar base flow in a somewhat arbitrary

manner, we focus on the trajectory departing from the ES and follow its path towards the turbulent core. To investigate the dependence of turbulence growth dynamics on the choice of the initial condition, we conducted comparative simulations using the following initial disturbance:

$$\Psi = \epsilon f(y) \left(\frac{x'}{l_x}\right) z' \exp\left[-\left(\frac{x'}{l_x}\right)^2 - \frac{z'}{l_z}\right]^2 \quad (3.13)$$

$$(v'_x, v'_y, v'_z) = \left(-\frac{\partial\Psi}{\partial y} \sin\theta, \frac{\partial\Psi}{\partial z'}, -\frac{\partial\Psi}{\partial y} \cos\theta\right) \quad (3.13)$$

$$(x', z') = \left(\left(x - \frac{L_x}{2}\right)\cos\theta - \left(z - \frac{L_z}{2}\right)\sin\theta, \left(x - \frac{L_x}{2}\right)\sin\theta + \left(z - \frac{L_z}{2}\right)\cos\theta\right) \quad (3.13)$$

$$f(y) = (1 + y)^p (1 - y)^q \quad (3.13)$$

with  $p = q = 2$ ,  $\theta = 0$ ,  $\epsilon = 0.20970$ ,  $l_x = 2.1$ ,  $l_z = 0.7$  on the laminar state. (3.13) was adopted from the earlier bypass transition study of Agarwal *et al.* [1], although for the difference in the domain size, the trajectories we generate should not be considered a direct comparison.

Time series of the transition process (fig. 3.14) is qualitatively similar as those of the ES-initiated trajectories fig. 3.1, where the transition starts with an overshoot of the RSS followed by that of the TKE before decaying into the turbulent core. In the state space projection of fig. 3.15, trajectories initiated from the disturbance of (3.13) do not closely follow the unstable manifold of the ES (as approximated by the ES-initiated trajectories) at the beginning, but after the overshoot all trajectories seem to decay to the turbulent core in a similar manner. There are “knots” in both fig. 3.14 and fig. 3.15, corresponding to moment i and ii. In fig. 3.15, it seems that the trajectory tends to move towards the edge state, although finally it only lingers in the near region for a short time then quickly leaves. From fig. 3.16, streaks begin to form since moment ii.

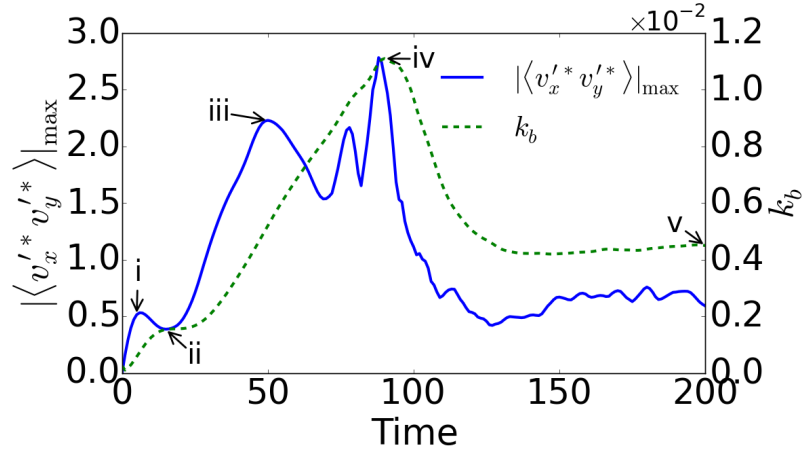


Figure 3.14: Time series of the transient growth of turbulence from the initial disturbance of (3.13) in Newtonian flow. The green dash line (left axis) shows bulk-average TKE; the blue solid line (right axis) shows peak values of instantaneous RSS profile.

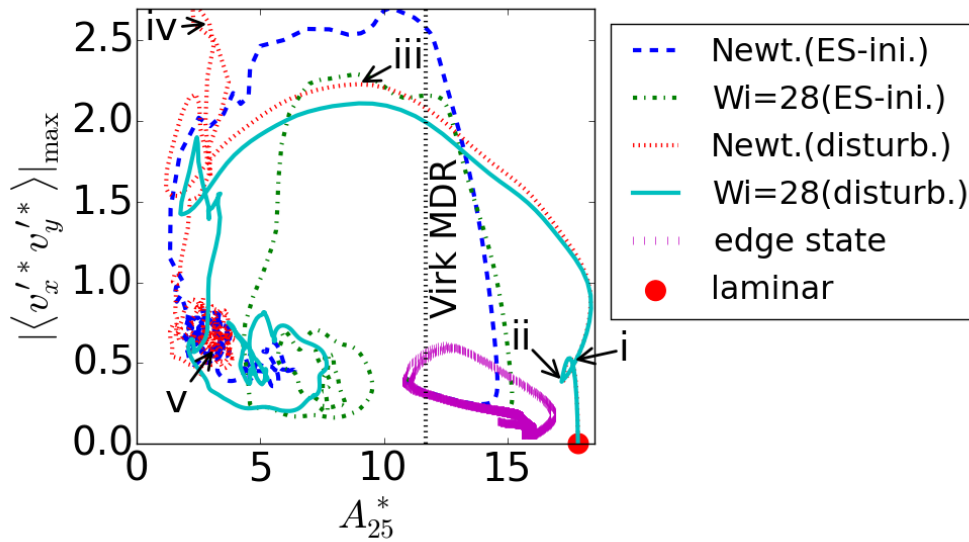


Figure 3.15: State-space projection of transient DNS trajectories initiated from the ES and from the imposed disturbance of (3.13).

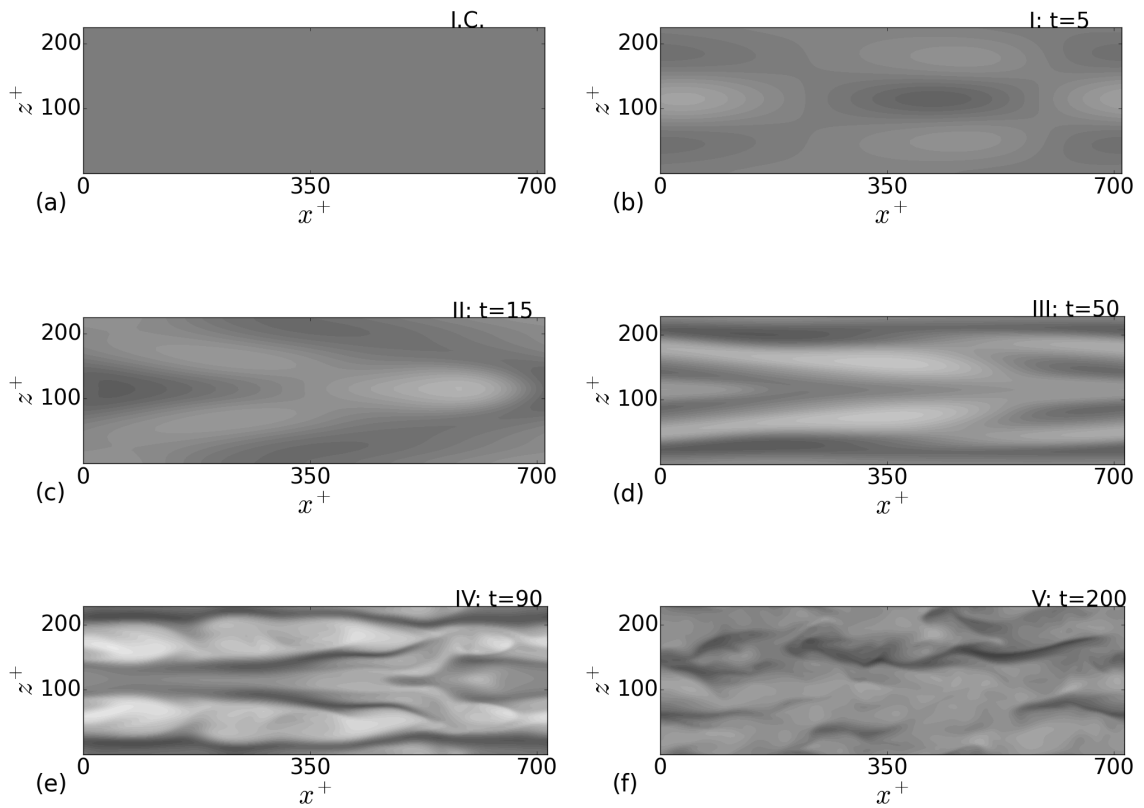


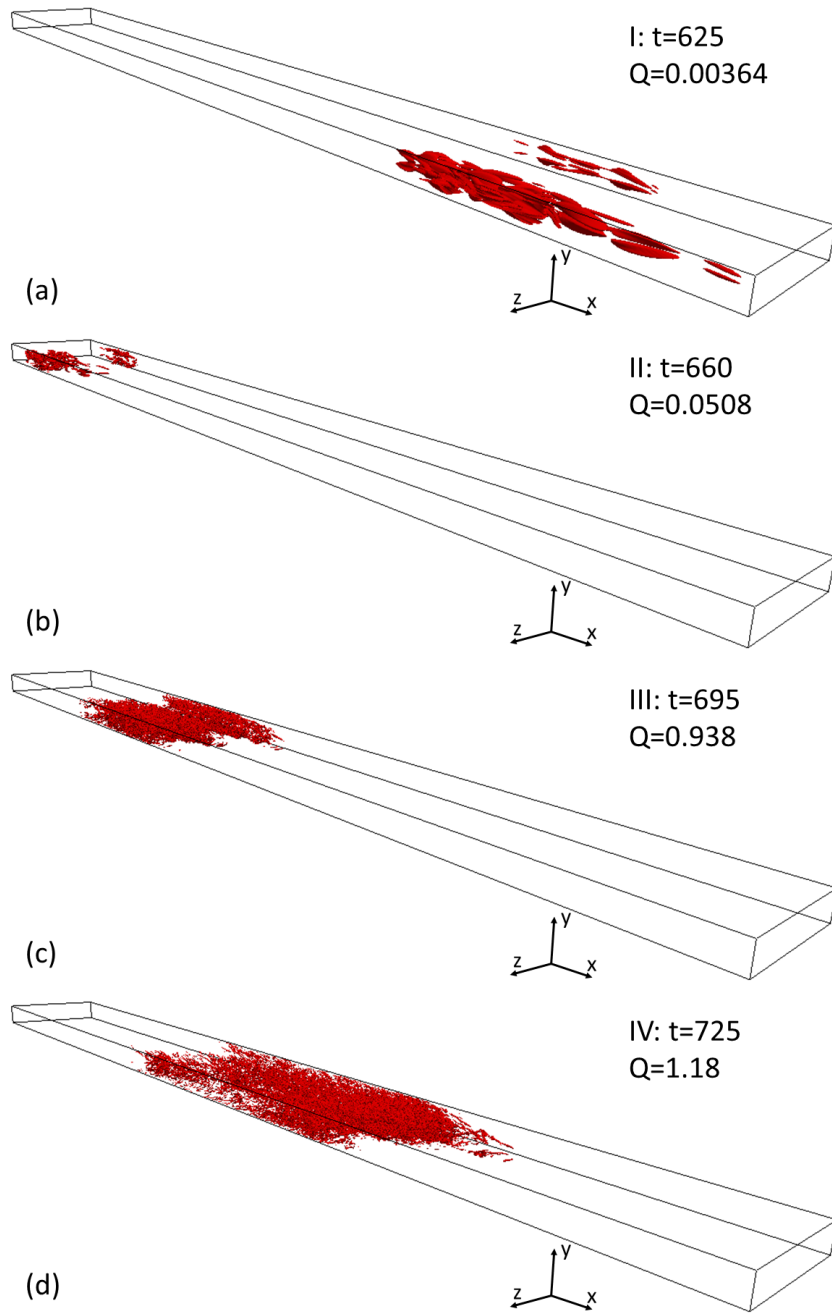
Figure 3.16: Streamwise velocity distribution at  $y^+ = 24.85$  for the transient development of Newtonian turbulence initiated from the imposed disturbance of (3.13): (a) is the initial disturbance; (b)–(f) are moments i–v labeled in fig. 3.14

## 3.2 Studies on the large domain

### 3.2.1 Flow structure development

In the Newtonian flow (shown in fig. 3.17), departing from ES, the weak turbulent spot is strengthened by initially congregating the vortex pairs (fig. 3.17(a)) Then these “unit vortex pairs” grow and break down, promoting the growth of an even more distinct turbulent spot, constituted by even denser and more tiny vortex structures, and meanwhile  $Q_{\text{rms}}$  keeps increasing (fig. 3.17(b)(c)). Then this spot expands to an extent and  $Q_{\text{rms}}$  stays at quite a steady level (fig. 3.17(d)). The spot region continues spreading, but at the same time a splitting attempt can be easily observed (fig. 3.17(e)). Tiny vortex structures of high density accumulate at two ends (in streamwise direction) of the turbulent spot, whereas sparser vortex structures are distributed in the middle. As the turbulent spot remains spreading, the proportion of the “sparse region” is also enlarged, which seems to cause thorough splitting within the spot region. However, two ends of the spot are joined in advance of the complete splitting, finally leading to the turbulent spot spreading all over the domain, and vortex structures are evenly redistributed (fig. 3.17(f)). Moreover,  $Q_{\text{rms}}$  also depressed in the sustained Newtonian turbulence.

Initiated from the same ES, a viscoelastic case of  $Wi = 64$  is compared with the Newtonian case. There is no significant difference between two cases at the beginning stage of L-T transient process (fig. 3.18(a)(b)). But whereafter it can be observed that vortex structures in  $Wi = 64$  case are not so dense or tiny as those in Newtonian case, though a splitting attempt is also distinct (fig. 3.18(c)). Then still similarly with Newtonian case, the initial localized turbulent spot keeps spreading as well as splitting,



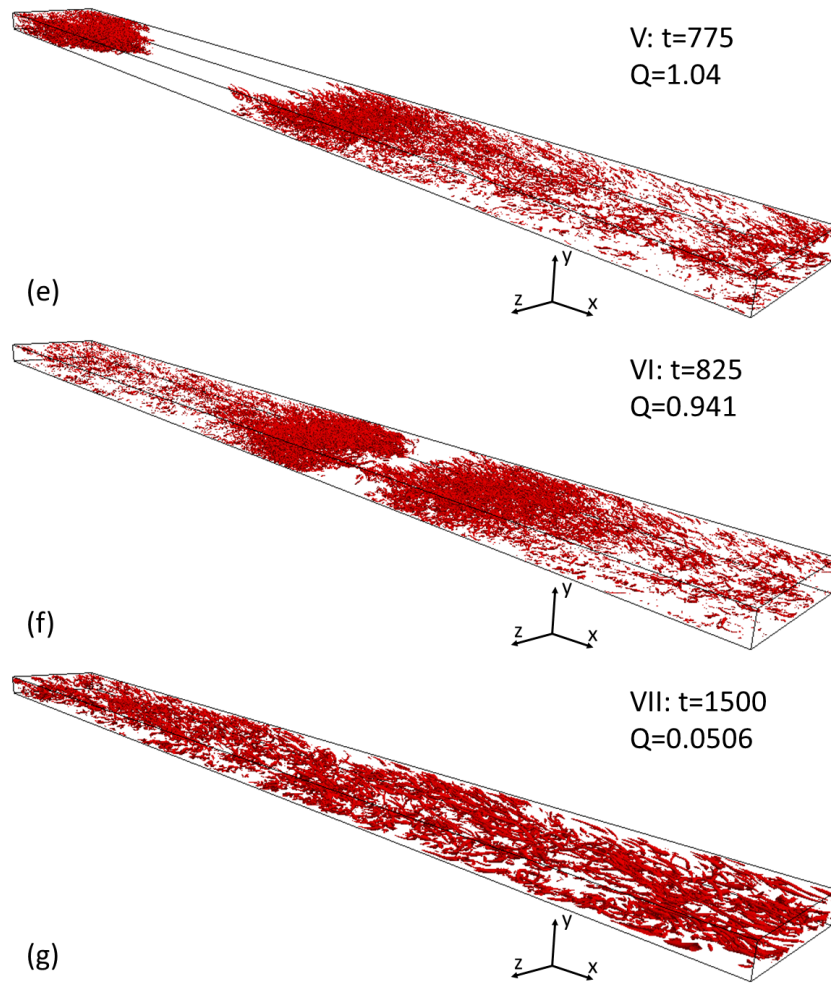
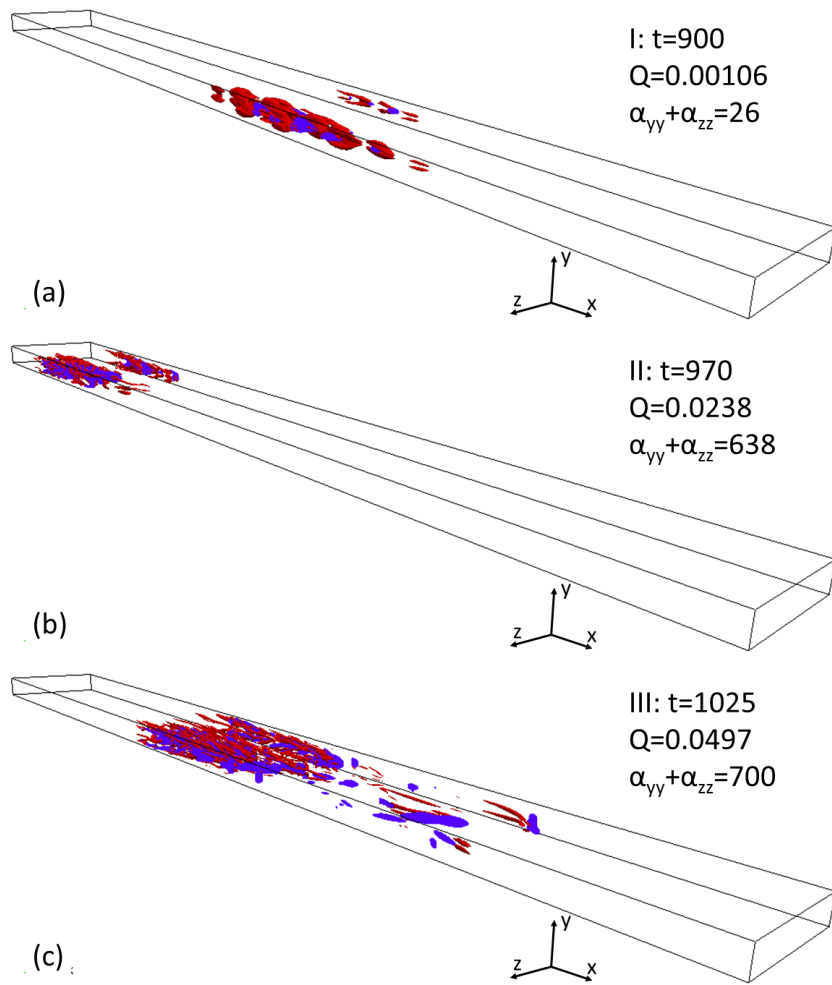


Figure 3.17: Vortex configuration for the Newtonian case: (a)–(g) are moments I–VII; the isosurface of  $Q = Q_{\text{rms}}$  is shown, where  $Q_{\text{rms}}$  is the root mean square of the  $Q$  field.



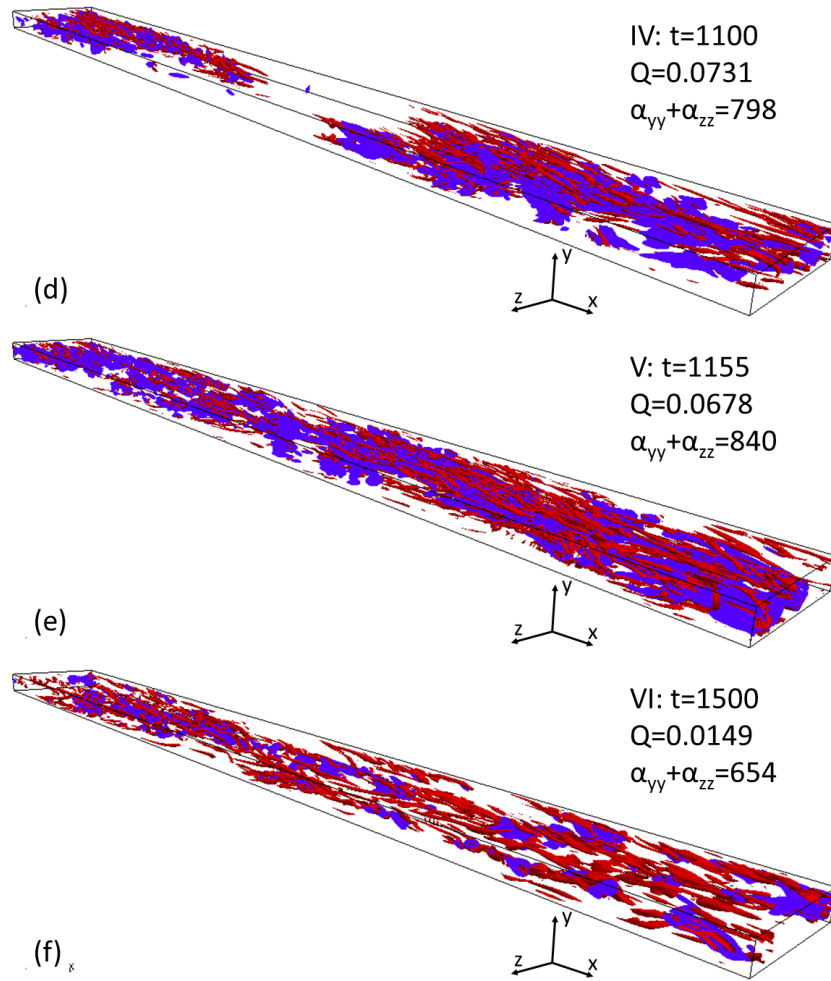


Figure 3.18: Vortex configuration for  $Wi = 64$  case: (a)–(f) are moments I–VI; the isosurface of  $Q = Q_{\text{rms}}$  is shown in red, where  $Q_{\text{rms}}$  is the root mean square of the  $Q$  field; the isosurface of  $\alpha_{yy} + \alpha_{zz} = 0.2(\alpha_{yy} + \alpha_{zz})_{\text{max}}$  is shown in blue.

thus here forms a region with two ends (in streamwise direction) composed of dense vortex structures and the middle part where only lower vortex strength is distributed (fig. 3.18(d)). And likewise, the spot region gradually expands by stretching its both ends and expanding the middle part. Although only with sparsely distributed vortex structures in this part, before it splits apart, two ends of the spot region has joined together (fig. 3.18(e)). Finally, this “self-combined” spot successfully spreads over the whole domain (fig. 3.18(f)). Additionally, during the transient process, except for the larger vortex structures in  $Wi = 64$  case,  $Q_{\text{rms}}$  drops to a much lower level compared to the Newtonian case. Also, such clear difference in  $Q$  between two ends of turbulent spot and the middle part is blurred in viscoelastic case. It is indicated that the polymer addition markedly helps smooth the transient process.

Moreover, spatial distribution of turbulence-induced polymer extension is also shown in fig. 3.18 by the isosurface of  $\alpha_{yy} + \alpha_{zz}$ . Strong correlation between active turbulent region and turbulence-induced polymer extension is observed. That is, polymer additives only affect the region with higher vortex strength and influence regions with lower vorticity very little. It can also be noticed that the magnitude of polymer extension suddenly shoots up at Moment II, which is consistent with the earlier observation in MFU that polymer effects are negligible at the initial stage of bursting.

Besides concerned about the 3D isosurfaces of  $Q$ , we also calculate  $y - z$  averaged  $Q$  for each instant and then obtain a spatiotemporal distribution of  $Q$  (fig. 3.19). Lighter color corresponds to higher magnitude of  $Q$ . In the Newtonian case, a spot with high  $Q$  begins to stand out from  $t \approx 650$ , indicated by a bright white point. This point keeps growing until  $t \approx 700$ , then a branch kicks in. This branch, another spot with high  $Q$  in fact, travels away from the initial spot, though there is always a fuzzy region with low  $Q$  between the two, which means these two spots are not really

set apart. Concerned about the features of the turbulent spot we observe in fig. 3.17, obviously the two spots we see here corresponds to two ends of the whole turbulent spot region, and the lingering fuzzy region in between confirms this turbulent spot fails splitting. Although the middle part remains weak and expanding, finally two ends converge and a turbulent spot region covering the whole channel emerges. All these observation above is consistent with what we see in fig. 3.17. Difference in viscoelastic case seems more remarkable in fig. 3.19. Between two ends of the spot region, a weak middle part still exists but only takes up very limited space, leading to a much more homogeneous turbulent spot region till it spreads over the domain. Polymer additives smooth the  $Q$  distribution within the turbulent spot.

Obviously, the growth of a localized turbulent spot is the essential feature in L-T transition for large domains in both Newtonian and viscoelastic cases. Streamwise velocity distribution in the  $x-z$  plane at  $y^+ = 24.85$  is shown in fig. 3.20 and fig. 3.21. In the Newtonian case, at Moment I, two low-speed and two high-speed streaks can be seen, all of which are generally straight but slightly bend at  $x^+ \approx 6500$ . Then these “bends” become more conspicuous (Moment II) and furthermore aggregate together, forming a region filled with streak “wrinkles” (Moment III). This region is highly localized and keeps growing until the whole domain is full of “wrinkles”, thus sustained turbulence is obtained finally (Moment IV~VII). Similar evolution can be observed in  $Wi = 64$  case. However, consistent with what we conclude above, polymers smooth the transient process, causing much smoother “wrinkles” within the turbulent spot. It’s still easy to distinguish the turbulent spot, but the low-speed and high-speed streamwise velocity streaks can still be told apart, instead of almost twisting together as we see in the Newtonian case.

No matter in which case, what we are only concerned about is the turbulent spot

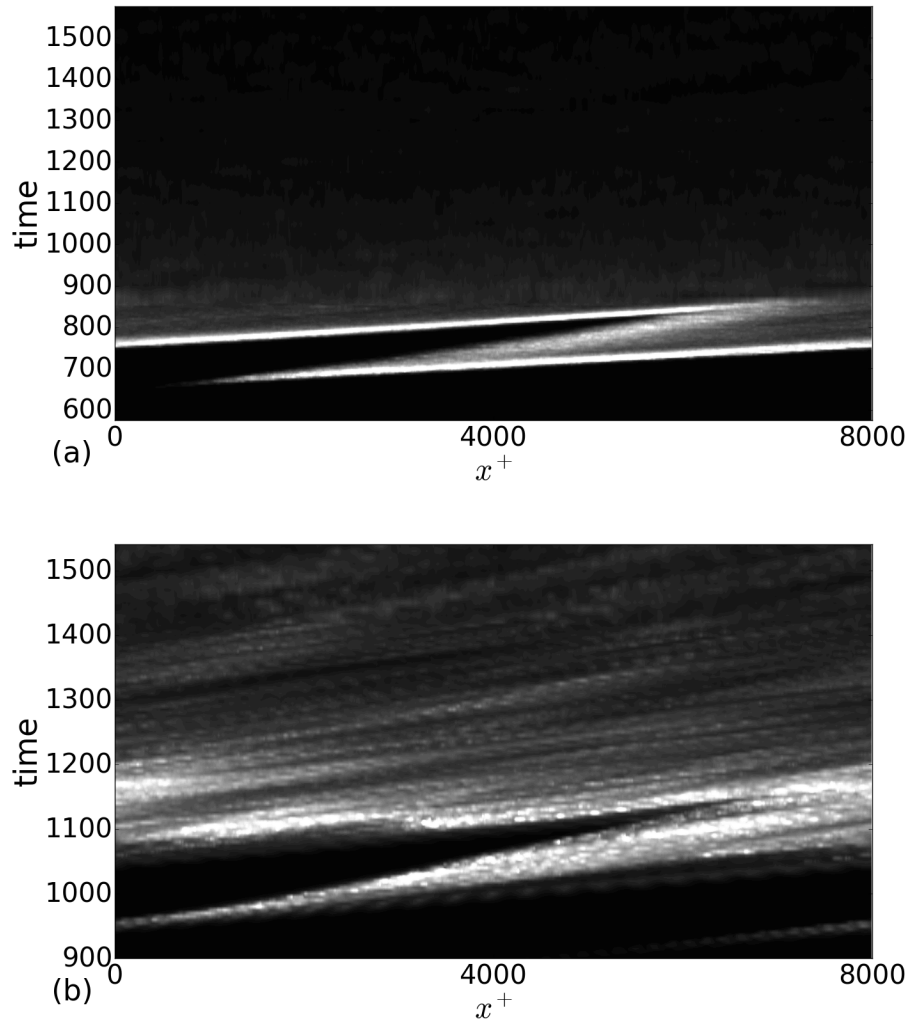


Figure 3.19: The spatiotemporal distribution of  $Q$ : (a)Newtonian; (b) $Wi = 64$ . The color ranges from black to white for 0 to 1.4 (a) and 0.75 (b), respectively.

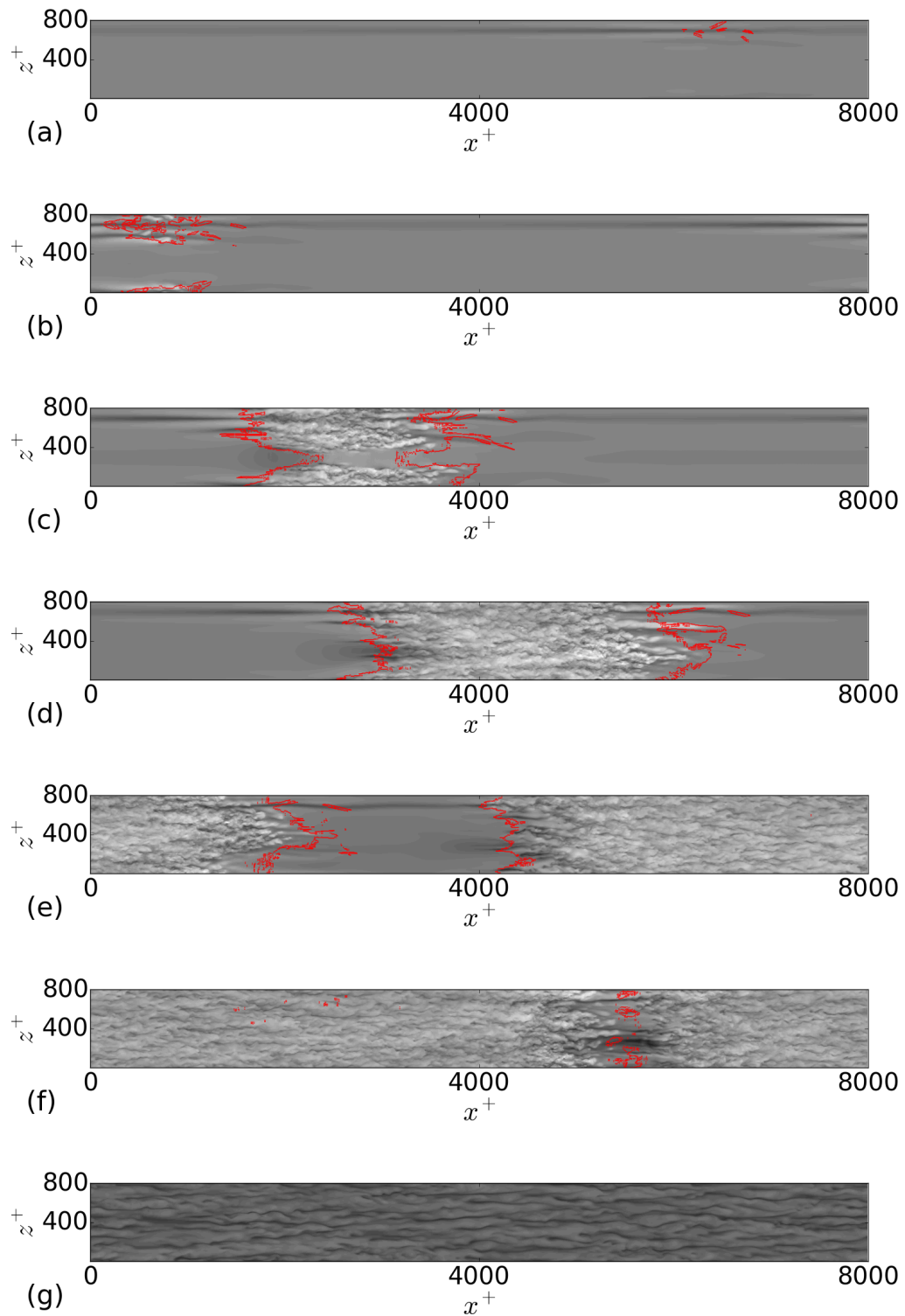


Figure 3.20: Streamwise velocity distribution at  $y^+ = 24.85$  for the Newtonian case: (a)~(g) – Moments I~VII; the color ranges from black to white for 0 to 1. Red lines indicate the boundary of laminar-turbulent regions.

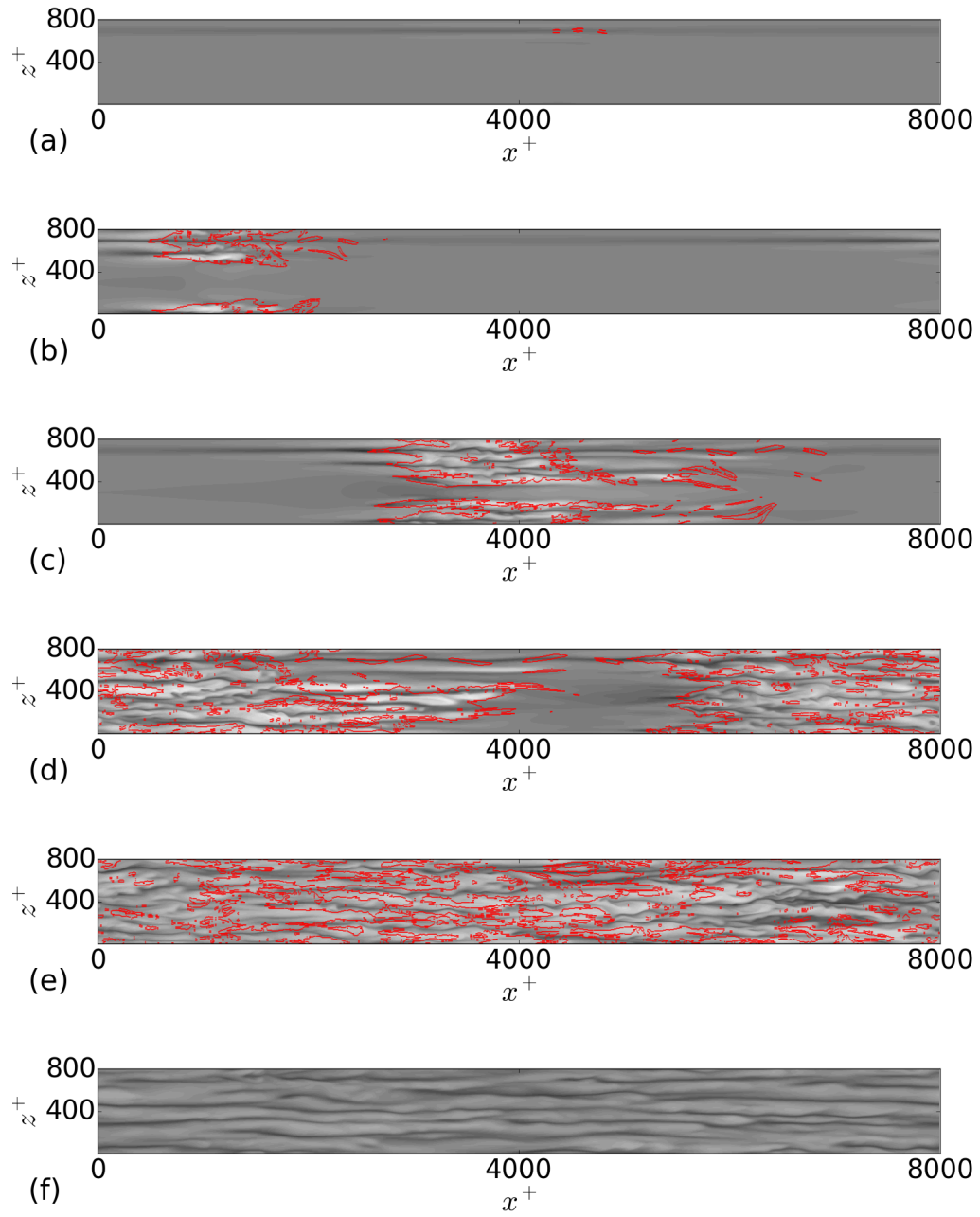


Figure 3.21: Streamwise velocity distribution at  $y^+ = 24.85$  for  $Wi = 64$  case: (a)~(f) – Moments I~VI; the color ranges from black to white for 0 to 1. Red lines indicate the boundary of laminar-turbulent regions.

region. According to fig. 3.20 and fig. 3.21, it is almost ordinary laminar state outside the turbulent spot region, and fig. 3.18 also confirms that it is only within this turbulent spot region that polymers make non-negligible effects. If we directly calculate the bulk flow statistics as usual, it can be deduced that these statistics would be massively influenced by these laminar regions, especially during the initial growth of the turbulent spot since most space of the domain is taken up by the laminar state. Allowing for this problem, we introduce a conditional averaged method for the following discussion. Firstly weighted average of  $Q$  in wall-normal direction is calculated to obtain a 2D array in  $x - z$  plane for  $\overline{Q_{xz}}$ . Then Ostu method[42] can be applied here to determine the threshold of laminar-turbulent region division[41]. The Ostu method can automatically select the threshold for picture segmentation, guaranteeing the picture is separated into two classes so that the intra-class variation is minimal or equivalent and the inter-class variation is maximal. Here, it's convenient to choose the threshold for dividing  $\overline{Q_{xz}}$  into two classes in Ostu method, thus the  $x - z$  plane can be separated into two regions: laminar region and turbulent region. We only analyze the turbulent region and neglect the laminar region. In particular, the same threshold is chosen for all moments in each case, which is determined as the average threshold for ten moments in sustained turbulence. And no L-T division is made in wall-normal direction. L-T boundaries are marked with red lines in fig. 3.20 and fig. 3.21. These turbulent regions circled by red lines are well consistent with the distribution of streak "wrinkles".

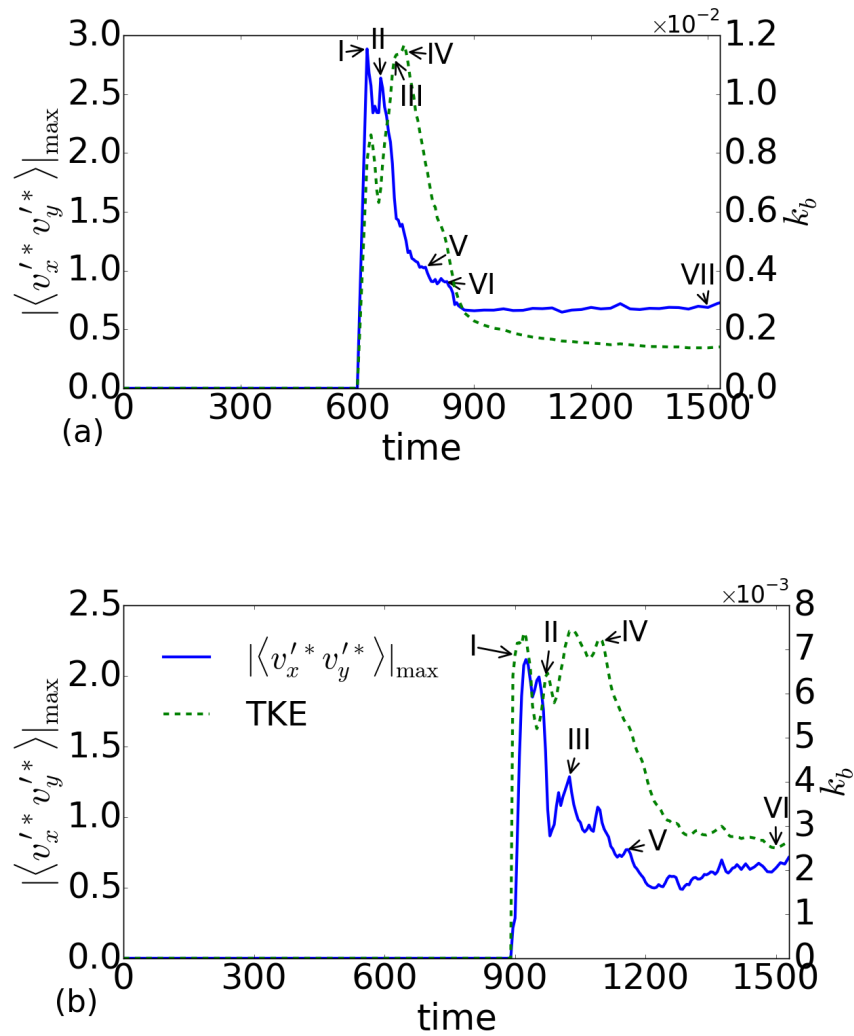


Figure 3.22: Time series of shooting trajectories initiated from the ES for  $L_x^+ \times L_z^+ = 8000 \times 800$  domains (conditional average): (a) Newtonian; (b)  $Wi = 64$ . The blue solid line (left axis) shows peak values of instantaneous RSS profile; the green dash line shows bulk-average TKE.

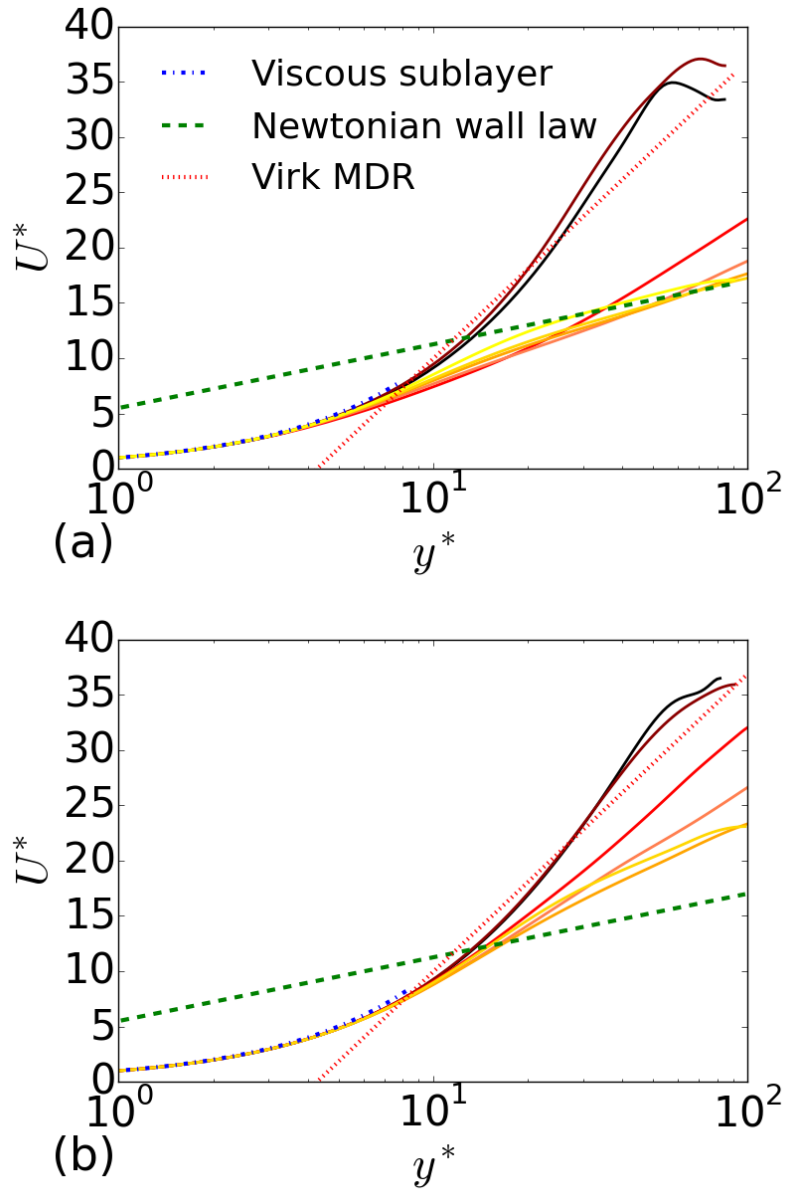
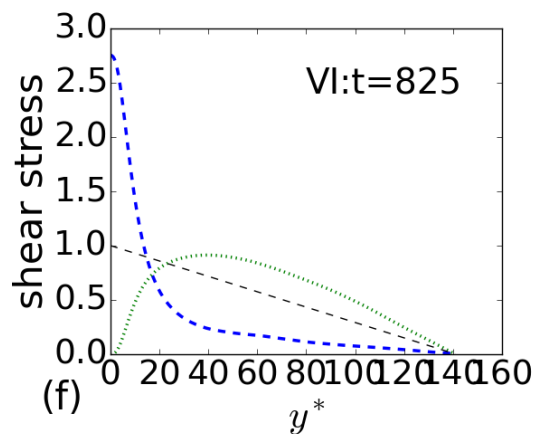
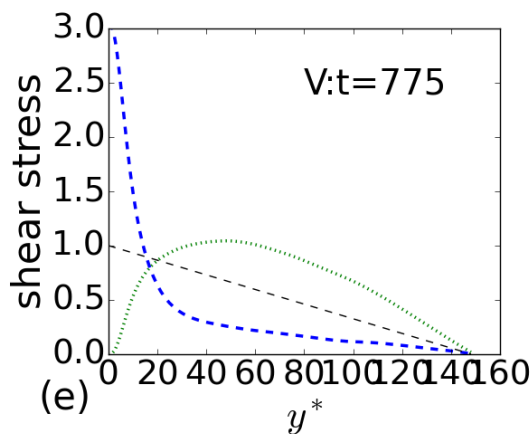
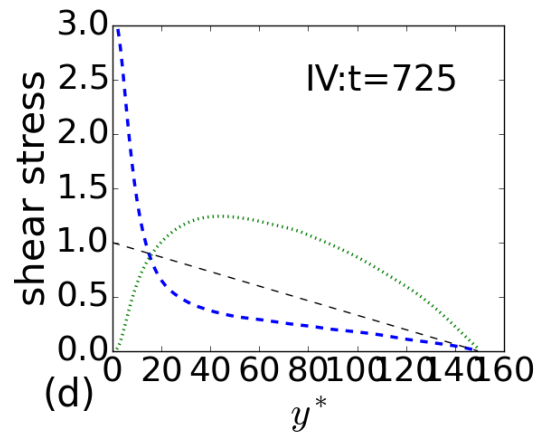
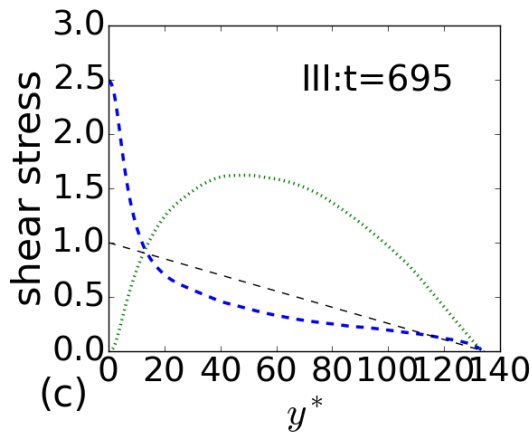
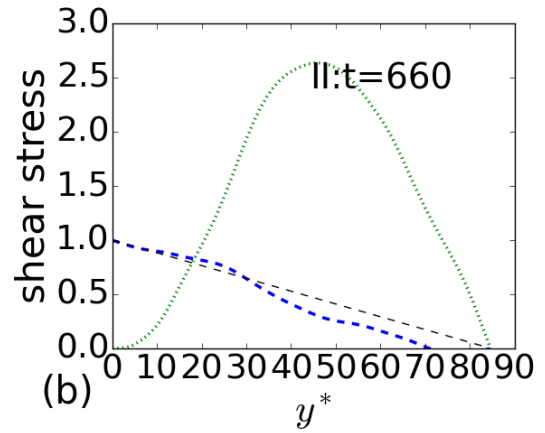
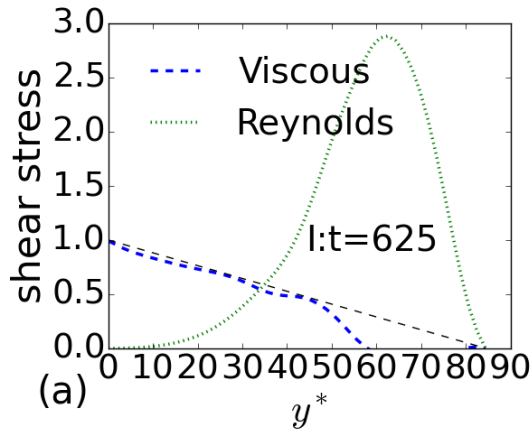


Figure 3.23: Mean velocity instantaneous profiles (conditional averaged): (a) Newtonian; (b)  $Wi = 64$ . The darker red lines indicate earlier moments and lighter yellow lines indicate later moments. All moments are marked in fig. 3.22. Dot-dashed: viscous sublayer; dashed: PvK log law; dotted: Virk log law.

### 3.2.2 Analysis based on conditional average

Time series of conditional averaged Reynolds shear stress (RSS) and turbulent kinetic energy (TKE) profiles are shown in fig. 3.22. For the Newtonian case, ES is so close to laminar state that statistics keep zero at the beginning stage. A sudden shoot-up follows, bringing both RSS and TKE to their first peaks at the same time (Moment I). Shortly after that, here comes a conjoint peak in RSS (Moment II). Corresponding to these moments, a turbulent spot composed of distinguishable vortex structure pairs emerges and grows. Then a pair of conjoint peaks in  $k_b$  comes up (Moment III and IV). At Moment III, those distinguishable vortex structures break into very dense and tiny vorticities, and  $Q$  explodes to a 20 times higher level. Then the turbulent region remains expanding. While both RSS and  $k_b$  peak off, corresponding to Moment V and VI, in the turbulent region there are three visible parts: two ends with dense vortex structures and a middle part with sparse structures. Finally, both trajectories drop to a steady level and sustained turbulence is obtained (Moment VII). For the  $Wi = 64$  case, both magnitudes of statistics are reduced to only  $\frac{2}{3}$  of those in Newtonian case, and secondary peaks become more conspicuous (such as peaks at  $t \approx 1000, 1100$  in RSS profile). But generally trajectories for the Newtonian case and viscoelastic case share similar features. A turbulent spot with growing vortex pairs is generated at the first shoot of the transition (Moment I), and this spot keeps growing until the conjoint RSS peak (Moment II). As for the following conjoint  $k_b$  peaks (Moment III and IV), the turbulent spot expands while the vortex pairs break down. Then the turbulent spot begins spreading as well as splitting attempt during the dropping of statistics (Moment V). Finally the turbulence is sustained with the turbulent spot spreading over the channel (Moment VI).



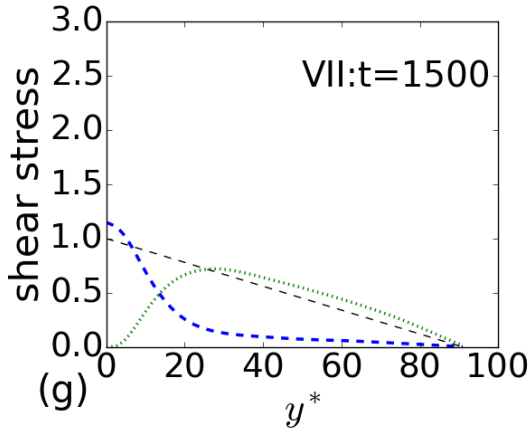


Figure 3.24: Contributions to the total shear stress (conditional averaged, bottom wall) in the Newtonian case: (a)~(g) – moments I~VII.

Mean velocity profiles are shown in fig. 3.23. In both cases, for the first stage of transition (Moment I and II),  $U_m$  almost keep the same magnitude within viscous wall region ( $y^+ < 50$ ). Then  $U_m$  gradually drops down when vortex structures begin to break down. When the turbulent spot expands to a level where splitting attempt become remarkable, again overlapping  $U_m$  profiles can be seen, until turbulence sustains itself and then the slope of  $U_m$  increases a little in buffer layer ( $5 < y^+ < 30$ ). Obviously, there are two overlapping periods above, which means two comparatively steady states in the whole L-T transition for large domains: corresponding to Moment I~II and Moment V~VI in the Newtonian case, and Moment I~II and Moment IV~V in  $Wi = 64$  case. In these two states, there is no intrinsic change but growing of the turbulent spot size.

The instantaneous profiles of contributions of total shear stress (TSS) (viscous shear stress (VSS), Reynolds shear stress (RSS) and polymer shear stress (PSS)) are shown in fig. 3.24 and fig. 3.25. Evolution of VSS and RSS seems qualitatively similar between Newtonian and viscoelastic cases. At moment I, RSS peaks in the outer

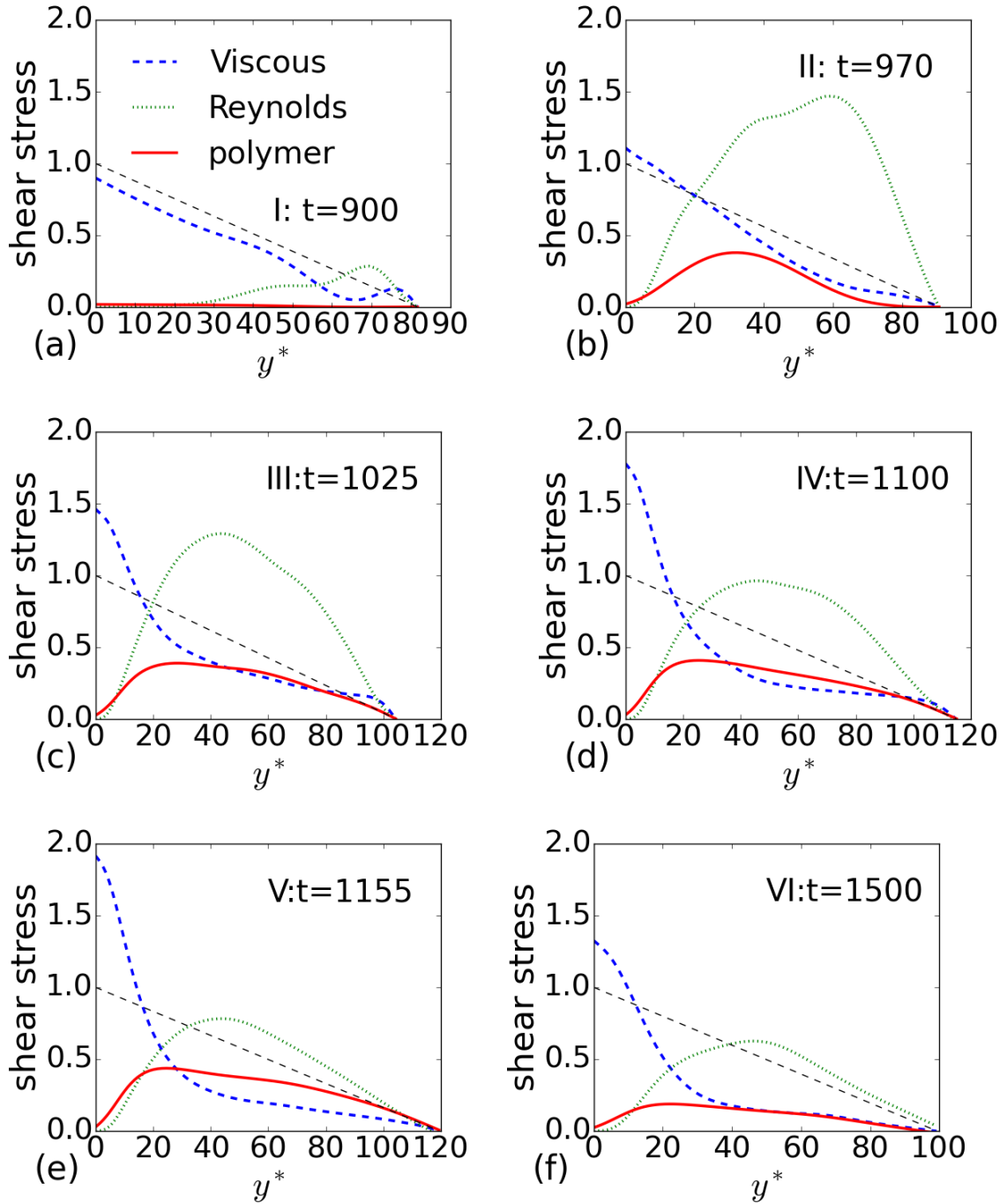


Figure 3.25: Contributions to the total shear stress (conditional averaged, bottom wall) in  $Wi = 64$  case: (a)~(f) – moments I~VI.

region ( $y^+ = 60 \sim 70$ ) while VSS is sizeable in the viscous wall region but rather small in the outer region. Then the peak of RSS gradually moves from the center region towards wall and the magnitude decreases during the whole process. The breakdown of vortex structures promotes a sudden shoot-up of VSS at the wall, and until sustained turbulence the value of VSS at the wall drops back. However, there are of course some differences with polymer addition except the depression of quantitative magnitudes. PSS cannot be neglected since prominent turbulent spot is generated and peaks in the buffer layer at Moment II. Then PSS remains at a comparable level with VSS at  $y = 30 \sim 90$  for the following transient process.

Finally, it is noted that the simulation results in this thesis can all be tested in experiments. Although an MFU does not exist in realistic flow conditions, taking an ergodic view of turbulence, the ensemble of states sampled in an MFU in the temporal dimension will be reflected in extended flow domains at different spatial locations. In particular, spatial intermittency of bursting events can be measured and compared with our simulation results. Meanwhile simulation results in the extended domain reported here already resonates with existing experiments of the L-T transition: e.g., Avila *et al.* [2], Barkley *et al.* [3].

# Chapter 4

## Conclusions

The transient problem of turbulence growth from the edge state and the polymer effects thereon are studied with DNS. In Newtonian flow, the transition starts with a strong overshoot of the Reynolds shear stress which results from the intensification of the streamwise velocity streams as well as the three-dimensional distortion of the primary vortices. As the RSS reaches the maximum, streak instability quickly leads to a breakdown of the primary vortices into a dense cloud of small but high-intensity eddies, at which the turbulent kinetic energy rises to its peak. These small-scale fluctuations also result in a sudden jump in the viscous dissipation rate, which quench the fluctuations and regulate the flow into the turbulent core. The introduction of drag-reducing polymers does not affect the initial growth of instability. However, it stabilizes the primary streak-vortex structures and prevents the breakdown into small-scale eddies. Significant polymer stress and conversion to elastic energy are only observed after the peak of TKE, where breakdown would happen in a Newtonian fluid. Throughout the whole process, polymers suppress turbulence generation and

there is no indication of elasticity-driven instability.

The lack of polymer effects during the initial growth of turbulence indicates that near the ES there is a state-space region where polymers do not suppress turbulence, which is the qualitative feature of MDR. In addition, as turbulence grows, the mean velocity profile in the near-wall region initially drops slowly, which suddenly speeds up as it passes the MDR level. The transient region near the ES is thus a promising direction to search for the origin of MDR.

In addition, a simple dynamical model of describing the statistically-converged is a three-stage cycle: (1) the flow samples the core of turbulence, which takes up the majority of turbulence life time in the Newtonian limit and becomes shortened as elasticity increases [75, 78]; (2) intermittent escape from the core takes the system near the ES – the so-called hibernating turbulence [75, 78, 74]; (3) as the flow is bounced back near the ES, it follows its unstable manifold and goes through a similar overshoot stage – which appears as bursting events – before returning to the turbulence core. Studying the polymer effects on the transient growth of turbulence also helps us understand the bursting dynamics in viscoelastic turbulence. In particular, the large magnitudes of polymer shear stress during this process would explain the conflicting observations in previous experimental and numerical studies.

It is also found that the choice of the initial disturbance has a non-trivial impact on the turbulence growth dynamics. Although trajectories totally differentiate from those initiated from ES in the transition process, they once tend to approach ES while surpassing the L-T boundary. This reveals non-neglectable significance of ES in L-T transition studies.

For the extended domains, a turbulent spot is initially formed, composed of low-intensity vortex structure pairs, instead of elongated tube-like structures in near MFUs. This turbulent spot grows, and Reynolds shear stress surpasses its first con-joint peaks(in the conditional averaged time series plot), then the vortex breakdown happens. The turbulent spot consisting of dense small-scaled vortex structures keeps spreading, while the turbulent kinetic energy is shooting up again. As the drop of  $k_b$ , the turbulent spot extends with a weak body and two strong ends, finally filling up the domain. Conditional averaged streamwise velocity profiles indicate that before the first RSS peak and shortly after the second  $k_b$  peak, the flow respectively maintains the same status within the turbulent regions. Comparing Newtonian and non-Newtonian case, polymers suppress the intensity of bursting in transition, and they won't make effect before Reynolds shear stress peak, both of which are consistent with observations in near MFUs.

# Bibliography

- [1] Agarwal, A., Brandt, L., and Zaki, T. A. (2014). Linear and nonlinear evolution of a localized disturbance in polymeric channel flow. *J. Fluid Mech.*, **760**, 278–303.
- [2] Avila, K., Moxey, D., de Lozar, A., Avila, M., Barkley, D., and Hof, B. (2011). The onset of turbulence in pipe flow. *Nature*, **333**, 192–196.
- [3] Barkley, D., Song, B., Mukund, V., Lemoult, G., Avila, M., and Hof, B. (2015). The rise of fully turbulent flow. *Nature*, **526**(7574), 550–553.
- [4] Bird, R. B., Curtis, C. F., Armstrong, R. C., and Hassager, O. (1987). *Dynamics of polymeric liquids*, volume 2. John Wiley & Sons, Inc., New York, 2nd edition.
- [5] Cvitanović, P. (2013). Recurrent flows: the clockwork behind turbulence. *J. Fluid Mech.*, **726**, 1–4.
- [6] De Angelis, E., Casciola, C. M., and Piva, R. (2002). DNS of wall turbulence: dilute polymers and self-sustaining mechanisms. *Comput. Fluids*, **31**, 495–507.
- [7] Draad, A. A., Kuiken, G. D. C., and Nieuwstadt, F. T. M. (1998). Laminar-turbulent transition in pipe flow for Newtonian and non-Newtonian fluids. *J. Fluid Mech.*, **377**, 267–312.

- [8] Dubief, Y. and Delcayre, F. (2000). On coherent-vortex identification in turbulence. *J. Turbul.*, **1**, 1–22.
- [9] Dubief, Y., White, C. M., Terrapon, V. E., Shaqfeh, E. S. G., Moin, P., and Lele, S. K. (2004). On the coherent drag-reducing and turbulence-enhancing behaviour of polymers in wall flows. *J. Fluid Mech.*, **514**, 271–280.
- [10] Dubief, Y., Terrapon, V. E., White, C. M., Shaqfeh, E. S. G., Moin, P., and Lele, S. K. (2005). New answers on the interaction between polymers and vortices in turbulent flows. *Flow Turbul. Combust.*, **74**, 311–329.
- [11] Dubief, Y., Terrapon, V. E., and Soria, J. (2013). On the mechanism of elasto-inertial turbulence. *Phys. Fluids*, **25**, 110817.
- [12] Duguet, Y., Willis, A. P., and Kerswell, R. R. (2008). Transition in pipe flow: the saddle structure on the boundary of turbulence. *J. Fluid Mech.*, **613**, 255–274.
- [13] Duguet, Y., Schlatter, P., and Henningson, D. S. (2009). Localized edge states in plane couette flow. *Phys. Fluids*, **21**, 111701.
- [14] Durbin, P. and Wu, X. (2007). Transition beneath vortical disturbances. *Annu. Rev. Fluid Mech.*, **39**, 107–128.
- [15] Escudier, M. P., Presti, F., and Smith, S. (1999). Drag reduction in the turbulent pipe flow of polymers. *J. Non-Newton. Fluid Mech.*, **81**, 197–213.
- [16] Gibson, J. F. (2014). Channelflow: A spectral Navier-Stokes simulator in C++. Technical report, U. New Hampshire. [Channelflow.org](http://Channelflow.org).
- [17] Gibson, J. F., Halcrow, J., and Cvitanović, P. (2008). Visualizing the geometry of state-space in plane Couette flow. *J. Fluid Mech.*, **611**, 107–130.

- [18] Giles, W. B. and Pettit, W. T. (1967). Stability of dilute viscoelastic flows. *Nature*, **216**, 470–472.
- [19] Graham, M. D. (2004). Drag reduction in turbulent flow of polymer solutions. In D. M. Binding and K. Walters, editors, *Rheology Reviews 2004*, pages 143–170. British Society of Rheology.
- [20] Graham, M. D. (2014). Drag reduction and the dynamics of turbulence in simple and complex fluids. *Phys. Fluids*, **26**, 101301.
- [21] Hansen, R. J. and Little, R. C. (1974). Early turbulence and drag reduction phenomena in larger pipes. *Nature*, **252**, 690.
- [22] He, S. and Seddighi, M. (2015). Transition of transient channel flow after a change in Reynolds number. *J. Fluid Mech.*, **764**, 395–427.
- [23] Henningson, D., Lundbladh, A., and Johansson, A. (1993). A mechanism for bypass transition from localized disturbances in wall-bounded shear flows. *J. Fluid Mech.*, **250**, 169–207.
- [24] Hoda, N., Jovanovic, M. R., and Kumar, S. (2008). Energy amplification in channel flows of viscoelastic fluids. *J. Fluid Mech.*, **601**, 407–424.
- [25] Hoda, N., Jovanovic, M. R., and Kumar, S. (2009). Frequency responses of streamwise-constant perturbations in channel flows of Oldroyd-B fluids. *J. Fluid Mech.*, **625**, 411–434.
- [26] Housiadas, K. D., Beris, A. N., and Handler, R. A. (2005). Viscoelastic effects on higher order statistics and on coherent structures in turbulent channel flow. *Phys. Fluids*, **17**, 035106.

- [27] Jacobs, R. and Durbin, P. (2001). Simulations of bypass transition. *J. Fluid Mech.*, **428**, 185–212.
- [28] Jeong, J. and Hussain, F. (1995). On the identification of a vortex. *J. Fluid Mech.*, **285**, 69–94.
- [29] Jimenez, J. (1987). Bifurcations and bursting in two-dimensional Poiseuille flow. *Phys. Fluids*, **30**, 3644–3646.
- [30] Jiménez, J. and Moin, P. (1991). The minimal flow unit in near-wall turbulence. *J. Fluid Mech.*, **225**, 213–240.
- [31] Jiménez, J., Kawahara, G., Simens, M. P., Nagata, M., and Shiba, M. (2005). Characterization of near-wall turbulence in terms of equilibrium and “bursting” solutions. *Phys. Fluids*, **17**, 015105.
- [32] Khapko, T., Kreilos, T., Schlatter, P., Duguet, Y., Eckhardt, B., and Henningson, D. S. (2016). Edge states as mediators of bypass transition in boundary-layer flows. *J. Fluid Mech.*, **801**, R2.
- [33] Kim, J., Moin, P., and Moser, R. (1987). Turbulence statistics in fully-developed channel flow at low Reynolds-number. *J. Fluid Mech.*, **177**, 133–166.
- [34] Kim, K., Li, C. F., Sureshkumar, R., Balachandar, S., and Adrian, R. J. (2007). Effects of polymer stresses on eddy structures in drag-reduced turbulent channel flow. *J. Fluid Mech.*, **584**, 281–299.
- [35] Kushwaha, A., Park, J. S., and Graham, M. D. (2017). Temporal and spatial intermittencies within channel flow turbulence near transition. *Phys. Rev. Fluids*.  
to appear.

- [36] Li, C. F., Sureshkumar, R., and Khomami, B. (2006). Influence of rheological parameters on polymer induced turbulent drag reduction. *J. Non-Newton. Fluid Mech.*, **140**, 23–40.
- [37] Li, W. and Graham, M. D. (2007). Polymer induced drag reduction in exact coherent structures of plane Poiseuille flow. *Phys. Fluids*, **19**, 083101.
- [38] Min, T., Yoo, J. Y., Choi, H., and Joseph, D. D. (2003a). Drag reduction by polymer additives in a turbulent channel flow. *J. Fluid Mech.*, **486**, 213–238.
- [39] Min, T., Choi, H., and Yoo, J. Y. (2003b). Maximum drag reduction in a turbulent channel flow by polymer additives. *J. Fluid Mech.*, **492**, 91–100.
- [40] Nishioka, M. and Asai, M. (1985). Some observations of the subcritical transition in plane poiseuille flow. *J. Fluid Mech.*, **150**, 441–450.
- [41] Nolan, K. P. and Zaki, T. A. (2013). Conditional sampling of transitional boundary layers in pressure gradients. *Journal of Fluid Mechanics*, **728**, 306–339.
- [42] Otsu, N. (1979). A threshold selection method from gray-level histograms. *IEEE Trans. Syst. Man. Cybern.*, **9**(1), 62–66.
- [43] Page, J. and Zaki, T. A. (2014). Streak evolution in viscoelastic Couette flow. *J. Fluid Mech.*, **742**, 520–551.
- [44] Park, J. S. and Graham, M. D. (2015). Exact coherent states and connections to turbulent dynamics in minimal channel flow. *J. Fluid Mech.*, **782**, 430–454.
- [45] Peyret, R. (2002). *Spectral methods for incompressible viscous flow*. Springer, New York.

- [46] Pope, S. B. (2000). *Turbulent flows*. Cambridge University Press, Cambridge, United Kingdom.
- [47] Procaccia, I., L'vov, V. S., and Benzi, R. (2008). Colloquium: theory of drag reduction by polymers in wall-bounded turbulence. *Rev. Mod. Phys.*, **80**, 225–247.
- [48] Ptasinski, P. K., Boersma, B. J., Nieuwstadt, F. T. M., Hulsen, M. A., van den Brule, B. H. A. A., and Hunt, J. C. R. (2003). Turbulent channel flow near maximum drag reduction: simulations, experiments and mechanisms. *J. Fluid Mech.*, **490**, 251–291.
- [49] Ram, A. and Tamir, A. (1964). Structural turbulence in polymer solutions. *J. Appl. Polym. Sci.*, **8**, 2751–2762.
- [50] Rolland, J. (2014). Turbulent spot growth in plane Couette flow: statistical study and formation of spanwise vorticity. *Fluid Dyn. Res.*, **46**(1), 015512.
- [51] Samanta, D., Dubief, Y., Holzner, M., Schäfer, C., Morozov, A. N., Wagner, C., and Hof, B. (2013). Elasto-inertial turbulence. *Proc. Natl. Acad. Sci. U. S. A.*, **110**, 10557–100562.
- [52] Schlatter, P., Brandt, L., de lange, H. C., and Henningson, D. S. (2008). On streak breakdown in bypass transition. *Phys. Fluids*, **20**, 101505.
- [53] Schneider, T. M., Eckhardt, B., and Yorke, J. A. (2007). Turbulence transition and the edge of chaos in pipe flow. *Phys. Rev. Lett.*, **99**, 034502.
- [54] Schneider, T. M., Gibson, J. F., Lagha, M., De Lillo, F., and Eckhardt, B. (2008). Laminar-turbulent boundary in plane Couette flow. *Phys. Rev. E*, **78**, 037301.
- [55] Schneider, T. M., Marinc, D., and Eckhardt, B. (2010). Localized edge states nucleate turbulence in extended plane Couette cells. *J. Fluid Mech.*, **646**, 441–451.

- [56] Skufca, J. D., Yorke, J. A., and Eckhardt, B. (2006). Edge of chaos in a parallel shear flow. *Phys. Rev. Lett.*, **96**, 174101.
- [57] Sreenivasan, K. R. and White, C. M. (2000). The onset of drag reduction by dilute polymer additives, and the maximum drag reduction asymptote. *J. Fluid Mech.*, **409**, 149–164.
- [58] Sureshkumar, R. and Beris, A. N. (1995). Effect of artificial stress diffusivity on the stability of numerical calculations and the flow dynamics of time-dependent viscoelastic flows. *J. Non-Newton. Fluid Mech.*, **60**, 53–80.
- [59] Sureshkumar, R. and Beris, A. N. (1997). Direct numerical simulation of the turbulent channel flow of a polymer solution. *Phys. Fluids*, **9**, 743–755.
- [60] Toh, S. and Itano, T. (2003). A periodic-like solution in channel flow. *J. Fluid Mech.*, **481**, 67–76.
- [61] Toms, B. A. (1948). Some observations on the flow of linear polymer solutions through straight tubes at large Reynolds numbers. In *Proc. 1st Int'l. Congress on Rheology*, volume 2, pages 135–141, Amsterdam.
- [62] Virk, P. S. (1975). Drag reduction fundamentals. *AIChE J.*, **21**, 625–656.
- [63] Wang, J., Gibson, J. F., and Waleffe, F. (2007). Lower branch coherent states in shear flows: transition and control. *Phys. Rev. Lett.*, **98**, 204501.
- [64] Wang, S. N., Graham, M. D., Hahn, F. J., and Xi, L. (2014). Time-series and extended Karhunen–Loève analysis of turbulent drag reduction in polymer solutions. *AIChE J.*, **60**, 1460–1475.

- [65] Warholic, M. D., Massah, H., and Hanratty, T. J. (1999). Influence of drag-reducing polymers on turbulence: effects of Reynolds number, concentration and mixing. *Exp. Fluids*, **27**, 461–472.
- [66] Warholic, M. D., Heist, D. K., Katcher, M., and Hanratty, T. J. (2001). A study with particles image velocimetry of the influence of drag-reducing polymers on the structure of turbulence. *Exp. Fluids*, **31**, 474–483.
- [67] Webber, G. A., Handler, R. A., and Sirovich, L. (1997). The Karhunen-Loève decomposition of minimal channel flow. *Phys. Fluids*, **9**, 1054–1066.
- [68] Whalley, R. D., Park, J. S., Kushwaha, A., Dennis, D. J., Graham, M. D., and Poole, R. J. (2017). Low-drag events in transitional wall-bounded turbulence. *Phys. Rev. Fluids*. to appear.
- [69] White, C. M. and Mungal, M. G. (2008). Mechanics and prediction of turbulent drag reduction with polymer additives. *Annu. Rev. Fluid Mech.*, **40**, 235–256.
- [70] White, C. M., Somandepalli, V. S. R., and Mungal, M. G. (2004). The turbulence structure of drag-reduced boundary layer flow. *Exp. Fluids*, **36**, 62–69.
- [71] Wu, X., Moin, P., and Hickey, J.-P. (2014). Boundary layer bypass transition. *Phys. Fluids*, **26**, 091104.
- [72] Wu, X., Moin, P., Adrian, R. J., and Baltzer, J. R. (2015). Osborne Reynolds pipe flow: Direct simulation from laminar through gradual transition to fully developed turbulence. *Proc. Natl. Acad. Sci. U. S. A.*, **112**, 7920–7924.
- [73] Xi, L. (2009). *Nonlinear dynamics and instabilities of viscoelastic fluid flows*. Ph.D. thesis, University of Wisconsin-Madison.

- [74] Xi, L. and Bai, X. (2016). Marginal turbulent state of viscoelastic fluids: A polymer drag reduction perspective. *Phys. Rev. E*, **93**.
- [75] Xi, L. and Graham, M. D. (2010a). Active and hibernating turbulence in minimal channel flow of Newtonian and polymeric fluids. *Phys. Rev. Lett.*, **104**, 218301.
- [76] Xi, L. and Graham, M. D. (2010b). Turbulent drag reduction and multistage transitions in viscoelastic minimal flow units. *J. Fluid Mech.*, **647**, 421–452.
- [77] Xi, L. and Graham, M. D. (2012a). Dynamics on the laminar-turbulent boundary and the origin of the maximum drag reduction asymptote. *Phys. Rev. Lett.*, **108**, 028301.
- [78] Xi, L. and Graham, M. D. (2012b). Intermittent dynamics of turbulence hibernation in Newtonian and viscoelastic minimal channel flows. *J. Fluid Mech.*, **693**, 433–472.
- [79] Zaki, T. and Durbin, P. (2005). Mode interaction and the bypass route to transition. *J. Fluid Mech.*, **531**, 85–111.
- [80] Zammert, S. and Eckhardt, B. (2014a). Periodically bursting edge states in plane Poiseuille flow. *Fluid Dyn. Res.*, **46**, 041419.
- [81] Zammert, S. and Eckhardt, B. (2014b). Streamwise and doubly-localised periodic orbits in plane Poiseuille flow. *J. Fluid Mech.*, **761**, 348–359.
- [82] Zhang, M., Lashgari, I., Zaki, T. A., and Brandt, L. (2013). Linear stability analysis of channel flow of viscoelastic Oldroyd-B and FENE-P fluids. *J. Fluid Mech.*, **737**, 249–279.